Astronomically-driven low-latitude climate variability across the onset of the Miocene Climatic Optimum

B.R. Spiering, BSc

Supervised by E. Wubben, MSc, prof. dr. A. Sluijs & dr. F.J. Hilgen

Department of Earth Sciences, Faculty of Geosciences, Utrecht University, Utrecht, The Netherlands

Abstract

Deep-sea records provide valuable information about high-latitude climate variability during the Miocene Climatic Optimum (MCO), however, records on tropical dynamics remain underrepresented. Therefore, the aim is to investigate the response of low-latitude climate to astronomical insolation forcing across the onset of the MCO. We present new high-resolution TEX_{86} and elemental records from Ocean Drilling Program Site 959 (eastern equatorial Atlantic Ocean) spanning ~2 Myr (~17.4-15.4 Ma) and analyse these together with other data from Site 959. Power spectral analysis reveals variability related to periods of ~10 m, ~2.5 m, ~1.5 m and ~0.5 m, corresponding to ~400 kyr eccentricity, ~100 kyr eccentricity, ~50 kyr cyclicity, and ~19-23 kyr precession, respectively. The astronomical age model is based on the correlation of bulk carbonate $\delta^{13}C$ minima to ~100 kyr eccentricity maxima, using biostratigraphy and isotope stratigraphy as initial age control. The ~50 kyr cycle originated from interference between precession and obliquity during which every second, and sometimes third, precession cycle was amplified by obliquity. Three phases with distinct climate variability were observed: (1) asymmetrical ~100 kyr variability before the MCO (~17.4-17 Ma), (2) strong obliquity forcing at the beginning of the MCO (~17-16.5 Ma) during a ~2.4 Myr eccentricity minimum, and (3) symmetrical ~100 kyr variability and ~400 kyr modulation in the later part of the MCO (~16.5-15.4 Ma). Our results indicate that climate at Site 959, before and during the MCO, was influenced by both regional monsoon dynamics and high-latitude (glacial) forcing.

1 Introduction

Deep-sea records provide valuable information about high-latitude climate variability, however, records on tropical dynamics during the Early/Middle Miocene remain underrepresented. Climate during the Early and Middle Miocene changed from an early (unipolar) icehouse world to a warmer climate state of the Miocene Climatic Optimum (MCO) (~17-15 Ma) (De Vleeschouwer et al., 2017; Miller et al., 2020; Westerhold et al., 2020). The MCO, referred to as an 'intermediate deep-time climate analogue' (Steinthorsdottir et al. 2021), provides a good opportunity to study monsoon dynamics in a warmer climate state, which is important considering global warming and the large population affected by monsoons.

Deep-sea records show that the Early/Middle Miocene climate was dynamic and responded to astronomically-forced changes in insolation mainly on ~100 and ~400 kyr eccentricity scales (Holbourn et al., 2007; 2015; Liebrand et al., 2016). Most atmospheric pCO_2 reconstructions for the MCO indicate levels of 400-600 ppm (Foster et al., 2012; Steinthorsdottir et al., 2019; Super et al., 2018; Zhang et al., 2013), although some studies suggest higher levels of ~800-1100 ppm (Sosdian et al., 2018; Stoll et al., 2019). The global mean surface temperature is estimated at ~23-25°C (Burls et al., 2021), significantly higher than today and near-future estimates (IPCC, 2021). Climate models generally fail to reconstruct the flattened surface temperature gradient and the full extent of the MCO warmth as indicated by proxy data (Burls et al., 2021), suggesting that some processes in the climate system are not fully understood yet.

To date, little is known about African monsoon dynamics during the Early and Middle Miocene and the transition across the onset of the MCO. Modelling experiments and sedimentary records covering more recent periods show that the North African monsoon responded strongly to astronomically forced changes in insolation (Bosmans et al., 2015a; Larrasoaña et al., 2003). During times of increased summer insolation, monsoonal winds, moisture transport and continental precipitation were intensified (Bosmans et al., 2015a). At low latitudes, insolation is mainly affected by climatic precession modulated by eccentricity, and to a small extent, by obliquity. However, obliquity can influence low-latitude climate through changes in inter-hemispheric insolation gradients (Bosmans et al., 2015b) or indirectly by remote high-latitude (glacial) forcing.

Therefore, the aim of this study is to investigate the response of low-latitude African climate to astronomical insolation forcing across the onset of the MCO. Previously presented Early/Middle Miocene sedimentary records from Ocean Drilling Program (ODP) Site 959 reveal well-expressed orbital cyclicity (Wubben et al., in prep.). This site is located in the eastern equatorial Atlantic Ocean, a region affected by the African monsoon. This indicates that Site 959 is very suitable for our aim. Here, we present new Early/Middle Miocene (~17.4-15.4 Ma) high-resolution TEX_{86} and elemental records (biogenic Ba, Fe/Al, V/Al) from ODP Site 959. These records can be used to reconstruct variations in sea surface temperature (SST), coastal upwelling, terrigenous sediment input and productivity, which are strongly related to monsoon dynamics. We analyse the new TEX_{86} and elemental records together with the records of bulk magnetic susceptibility (MS), bulk carbonate stable carbon and oxygen isotopic composition ($\delta^{13}C$ and $\delta^{18}O$), and weight% (wt%) $CaCO_3$ presented in Wubben et al. (in prep.). With this multi-proxy dataset we can investigate how different parts of the climate system responded to astronomical insolation forcing and how the response changed across the onset of the MCO. In light of future climate change, it is important to understand the sensitivity of the climate under higher atmospheric CO_2 concentrations and therefore understand the processes affecting SST.

2 Background

2.1 Miocene climate evolution

Sediment records from the tropical Pacific Ocean indicate that the onset of the MCO at 16.9 Ma was marked by a sharp ~1‰ decrease in benthic and bulk carbonate oxygen isotopic composition ($\delta^{18}O$), coinciding with a ~0.6‰ decrease in benthic and bulk carbonate carbon isotopic composition ($\delta^{13}C$) and a drop in $CaCO_3$ percentages (Holbourn et al., 2015). This indicates an intense perturbation of the carbon cycle, with increased carbonate dissolution and shoaling of the carbonate compensation depth (CCD). The negative $\delta^{13}C$ excursion is followed by a rapid recovery and onset of a long-lasting positive $\delta^{13}C$ excursion recognized globally in planktic and benthic foraminiferal records, called the Monterey Excursion (16.7-13.5 Ma) (Flower & Kennett, 1993; Holbourn et al., 2007; 2014; 2015; Vincent & Berger, 1985; Woodruff & Savin, 1991). Starting from 14.6 Ma, a stepwise cooling and/or expansion of the Antarctic Ice Sheet occurred, evident from sustained increases in $\delta^{18}O$, called the Middle Miocene Climatic Transition (MMCT) (Holbourn et al., 2013). The Monterey Hypothesis linked the MMCT to drawdown of pCO_2 due to enhanced organic carbon burial in a cooling climate (Vincent & Berger, 1985). Although, recently it was proposed that organic carbon burial increased due to drowning of continental shelfs related to elevated volcanic carbon emissions, global warming and sea level rise (Sosdian et al., 2020).

Most atmospheric pCO_2 reconstructions for the MCO indicate levels of 400-600 ppm (Foster et al., 2012; Steinthorsdottir et al., 2019; Super et al., 2018; Zhang et al., 2013), although some studies suggest higher levels of ~800-1100 ppm (Sosdian et al., 2018; Stoll et al., 2019). The MCO was significantly warmer than today and near-future estimates (IPCC, 2021), with a global mean surface temperature of ~23-25°C and a weakened equator-to-pole temperature gradient (Burls et al., 2021). SST reconstructions indicate an average of 26-30°C for the middle- to high latitude North Atlantic (Super et al., 2020) and 30°C for the eastern tropical Indian Ocean (northwest of Australia) (Sosdian & Lear, 2020). A bottom water temperature of 11°C was found for the Indian Ocean, ~9°C warmer than present (Modestou et al., 2020). Climate models generally fail to reconstruct the flattened surface temperature gradient between the tropics and midlatitudes and the full extent of the MCO warmth as indicated by proxy data (Burls et al., 2021). Simulations with ~850 ppm pCO_2 successfully reconstructed the MCO global mean surface temperature estimate of ~23°C, however, cold SST biases remained in the North Atlantic and Indian Ocean, while the tropics warmed too much (Burls et al., 2021).

Across the MMCT, in the Indian Ocean, tropical average SST decreased ~2°C (Sosdian & Lear, 2020) and bottom water temperatures decreased ~3°C, resulting in a bottom water $\delta^{18}O$ increase of ~0.6‰ (Modestou et al., 2020). The equator-to-pole temperature gradient steepened (Herbert et al., 2016) and atmospheric pCO_2 reconstructions indicate a decline of ~100-200 ppm across the MMCT (Foster et al., 2012; Sosdian et al., 2018; Steinthorsdottir et al., 2019; Super et al., 2018; Zhang et al., 2013).

Climate variability during the MCO was primarily paced by eccentricity, characterized by high-amplitude (~1‰) 100-kyr variations in benthic $\delta^{18}O$ and prominent 400-kyr variability in benthic $\delta^{13}C$ with superposed 100-kyr variations (Holbourn et al., 2007; Holbourn et al., 2014). Warming pulses, expressed by decreases in $\delta^{18}O$, coincided with negative shifts in $\delta^{13}C$ and were paced by 100-kyr eccentricity (Holbourn et al., 2014). These transient warmings concurred with increases in carbonate dissolution (Holbourn et al., 2014) and might be related to the large ~200 ppm variations in CO_2 reaching levels of >780-1100 ppm observed by Sosdian et al. (2018). An aberrant warming pulse occurred at 15.6 Ma, perhaps

superimposed on Milankovitch variability, coinciding with maxima in eccentricity (100 kyr, 400 kyr, and 2.4 Myr amplitude modulation) and obliquity (1.2 Myr modulation) (Holbourn et al., 2013) and paced by precession (Holbourn et al., 2014). This implies insolation to be a contributing trigger in the MCO transient warmings. Benthic $\delta^{18}O$ responded strongly to precession with lowest values occurring during high eccentricity when Earth reached perihelion in January (De Vleeschouwer et al., 2017). This suggests that Antarctic ice cover and/or deep water temperature (represented by benthic $\delta^{18}O$) was mainly dependent on southern hemisphere summer insolation.

2.2 Regional setting

The latitudinal position of the Intertropical Convergence Zone (ITCZ) shifts seasonally following sensible heating over the continent (Figure 1). During boreal summer, the ITCZ is centered over the North African continent at ~18°N (Trauth et al., 2009). Southwest (SW) monsoons carry moisture from the tropical Atlantic into North Africa, converging with the dry northeast (NE) trades at the ITCZ. Here, dust is mobilized and transported westward by the Saharan Air Layer (SAL) at mid-tropospheric levels (Trauth et al., 2009). During boreal winter, the ITCZ shifts southward to the Guinea coast and into the southern hemisphere African continent. Surface airflow over North Africa is dominated by the NE trades. A specific part of the NE trades, the Harmattan, transports dust from the Bodélé depression in Chad to the equatorial Atlantic (Prospero et al., 2002; Stuut et al., 2005; Trauth et al., 2009).

The Comoé River discharges into the Gulf of Guinea on the east side of Ivory Coast. However, sediment transport is effectively canalized, probably since the Oligocene, and therefore does not significantly influence Site 959 (Wagner, 1998). The main currents in the equatorial Atlantic are the westward flowing North Equatorial Current (NEC) and South Equatorial Current (SEC) and the eastward flowing Equatorial Undercurrent (EUC) (Norris, 1998a) (Figure 1). The EUC carries cool, saline water from the South Atlantic and is deflected northward into the Gulf of Guinea, producing a strong thermocline (Norris, 1998a). The Guinea current flows eastward into the Gulf of Guinea and is enforced by the North Equatorial Countercurrent (NECC) during boreal summer when the ITCZ moves northward (Norris, 1998a). Prior to the establishment of the Guinea Current at ~5 Ma, it was hindered by a too southerly position of the Guinea coast (<2.5°N) (Norris, 1998a). In the eastern equatorial Atlantic, oceanic upwelling occurs along the Equatorial Divergence Zone (Wagner, 1998) and wind-induced coastal upwelling occurs off Ivory Coast and Ghana during boreal summer due to the combination of the Guinea Current and winds flowing parallel along the coast (Vallé et al., 2017; Wagner, 1998). A minor coastal upwelling event occurs during boreal winter due to the displacement of the ITCZ and corresponding wind systems (Wagner, 1998; Wagner, 2002). Present-day SST in the Gulf of Guinea varies seasonally between ~25°C in summer and ~29°C in winter (Djakouré et al., 2017).

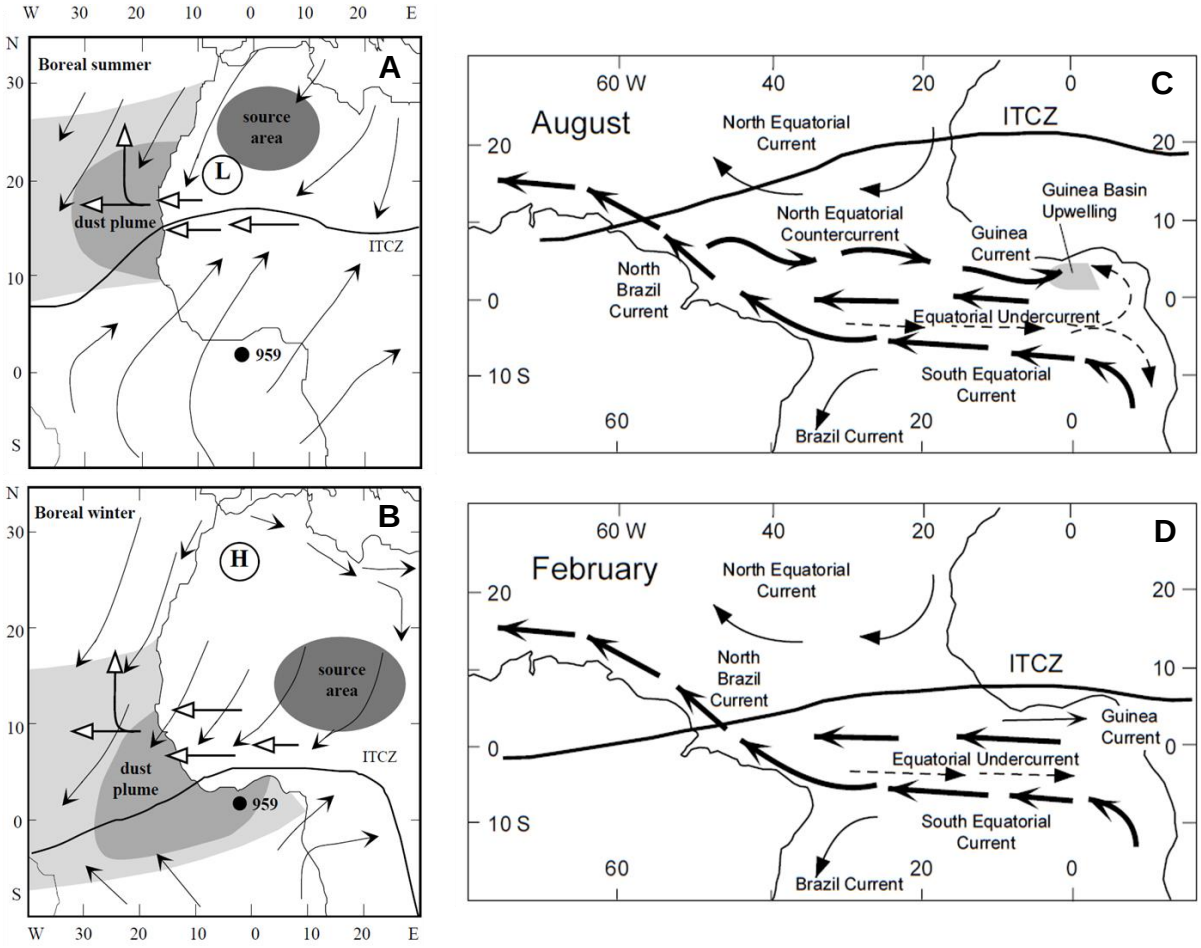

Figure 1. Generalized atmospheric circulation patterns (A-B) (Wagner, 1998) and major currents (C-D) (Norris, 1998a) during boreal summer and winter in the region around Site 959. A-B: Solid arrows = surface wind, open arrows = mid-level African Easterly Jet (AEJ) and Saharan Air Layer (SAL), dark grey shaded area = dust source area, light grey shaded area = seasonal dust plume. C-D: Solid arrows = surface currents , dashed arrows = undercurrents.

3 Material and methods

3.1 Material collection and site information

The material was collected during ODP Leg 159 at Site 959 hole A, located at 2102 m water depth in the eastern equatorial Atlantic Ocean ~120 km offshore of Ivory Coast (3°37'39.5''N, 2°44'6.7''W) (Figure 1) (Mascle et al., 1996). Site 959 is located on the southern edge of the Deep Ivorian Basin (DIB), just north of the top of the Côte d'Ivoire-Ghana Marginal Ridge (CIGMR). The CIGMR and DIB were formed due to the opening of the equatorial Atlantic during the early Cretaceous (Basile et al., 1993). At 17 Ma, Site 959 was located at a latitude of around 1°26'24''S (Van Hinsbergen et al., 2015).

Drilling at Site 959A resulted in a penetration of 480.7 m and an average core recovery of 94.9%. Shipboard and post-cruise age assessment suggest that a nearly complete Neogene section was recovered (Mascle et al., 1996; Norris, 1998b; Shafik et al., 1998; Vallé et al., 2017). The relatively shallow bathymetric position near the top of the marginal ridge allowed the recovery of relatively unaltered and undisturbed sediments.

This study focusses on Early to Middle Miocene sediments from cores 22X-26X (~218-268 rmbsf), retrieved using an Extended Core Barrel (XCB). The lithology was described as nannofossil chalk and clay, with interbedded diatomite in the lower part (23-26X) (Mascle et al., 1996). Alternations in sediment color were observed from light to dark, in which generally siliceous phases represent the darker lithology and clay/calcareous phases represent the lighter lithology (Mascle et al., 1996). Individual lithologies range in thickness from 10 to 80 cm (Mascle et al., 1996).

A revised meters below sea floor (rmbsf) depth scale was established by assuming 50 cm gaps at core breaks, based on triple-cored intervals in the Pliocene part of the section (Vallé et al., 2017). The cores were sampled continuously at the Bremen Core Repository at ~2 cm intervals.

We used the bulk magnetic susceptibility (MS), bulk carbonate stable carbon and oxygen isotopic composition ($\delta^{13}C$ and $\delta^{18}O$) and wt% $CaCO_3$ records presented by Wubben et al. (in prep.). Additionally, we generated new records of GDGT distribution (incl. TEX_{86}) and elemental records. For the interval 22X-26X (~218-268 rmbsf), MS was measured on an average resolution of ~4 cm, bulk isotopic composition on ~5 cm resolution, elemental composition on ~30 cm resolution for cores 22X-23X and on ~10 cm resolution for cores 24X-26X, and GDGT distribution on ~10 cm resolution.

3.2 Glycerol dialkyl glycerol tetraethers (GDGTs)

At Utrecht University, the samples were freeze-dried and cleaned by scraping of the outer surface layer to avoid contamination. The samples were crushed using a mortar and pestle to a fine powder. 25 ml of dichloromethane (DCM):methanol (MeOH) (9:1, v/v) was added to ~5 g of powdered sample material, after which microwave extraction was performed at a temperature of 70°C. At least 1 blank solution was included per 21 samples, subjected to all steps of the procedure. The extract was separated from the sediment and 99 ng synthetic C_{46} GDGT (m/z 744) internal standard was added. The extract was concentrated under a flow of nitrogen until most of the solvent was removed. To remove residual water and sediment, the extract was filtered using a column plugged with extracted cotton wool and 1-1.5 cm of Na_2SO_4 powder. The filtered extract was concentrated in a 30°C heating block under a flow of nitrogen to remove all solvent, resulting in the total lipid extract (TLE).

The TLE was separated into different polarity fractions by alumina oxide (AlO_x) column chromatography. The column was plugged with extracted cotton wool and ~4 cm of AlO_x powder. Firstly, the apolar fraction was eluted using hexane:DCM (9:1, v/v), followed by the neutral fraction using hexane:DCM (1:1, v/v), and lastly the polar fraction using DCM:MeOH (1:1, v/v). The fractions were concentrated in a 30°C heating block under a flow of nitrogen to remove all solvent. The masses of the fractions were determined by weighing the filled vials and subtracting the empty vial mass.

The polar fractions were dissolved in hexane:isopropanol (99:1, v/v) to a concentration of ~2 mg/ml. 50 µl of this fraction was filtered over a 0.45 µm polytetrafluoroethylene (PTFE) filter to remove any undissolved particles. Measurements were performed by high performance liquid chromatography – mass spectrometry (HPLC-MS) using an Agilent 1260 Infinity series HPLC coupled to an Agilent 6130 single-quadrupole mass spectrometer in selected ion monitoring (SIM) mode, following Hopmans et al. (2016). Peak areas in the mass chromatograms were calculated to determine relative GDGT abundances. For the terminology of isoprenoid and branched GDGTs we follow Sluijs et al. (2020) and Weijers et al. (2014).

The TetraEther indeX of tetraethers with 86 carbon atoms (TEX_{86}) is a proxy for annual mean SST, based on the relative abundance of four isoprenoid GDGTs produced by

Thaumarchaeota in the upper water column (Schouten et al., 2002). SST was reconstructed using the calibration of Kim et al. (2010), based on an extended marine core-top dataset and satellite-derived SST, excluding data from the Red Sea and (sub)polar oceans, applicable for SST >15°C:

$$TEX_{86}^{H} = \log TEX_{86} = \log \frac{[GDGT-2] + [GDGT-3] + [Cren']}{[GDGT-1] + [GDGT-2] + [GDGT-3] + [Cren']}$$

$$SST\ (°C) = 68.4\ TEX_{86}^{H} + 38.6\ (\pm 2.5°C)$$

The Branched and Isoprenoid Tetraether (BIT) index was used to track the contribution of terrestrially-derived isoprenoid GDGTs. The BIT is based on the relative abundance of branched GDGTs, which are mostly soil-derived, and crenarchaeol, which is dominantly marine-derived (Hopmans et al., 2004; adjusted to include branched GDGT isomers):

$$BIT = \frac{Ia + IIa + IIa' + IIIa + IIIa'}{Ia + IIa + IIa' + IIIa + IIIa' + Cren}$$

The BIT index mainly reflects fluvial transport of terrestrial organic matter (Hopmans et al., 2004). TEX_{86}-derived SSTs are considered unreliable for BIT values above 0.3 or 0.4 (Weijers et al., 2006).

Several other indices were calculated to assess potential biases in TEX_{86}-derived SSTs: Ring Index (RI) and ΔRI (Zhang et al., 2016), Methane Index (MI) (Zhang et al., 2011), GDGT-2/crenarchaeol ratio (Weijers et al., 2011), GDGT-0/crenarchaeol ratio (Blaga et al., 2009), GDGT-2/GDGT-3 ratio (Taylor et al., 2013), $\#rings_{tetra}$ (Sinninghe Damsté, 2016), and IIIa/IIa ratio (Xiao et al., 2016) (supplementary information).

3.3 Elemental records

Quantitative bulk elemental composition was measured with Inductively Coupled Plasma – Optical Emission Spectroscopy (ICP-OES) as described in Wubben et al. (in prep.). Biogenic barium (Ba_{bio}) is used as a proxy for export productivity (Dymond et al., 1992). At sites with significant terrestrial input, the barium signal in sediments may be strongly influenced by detrital barium present in aluminosilicates (Dymond et al., 1992). The Ba_{bio} signal was estimated by correcting the measured total Ba concentration for the detrital contribution (Dymond et al., 1992):

$$Ba_{bio} = Ba_{total} - \left(Al \times \left(\frac{Ba}{Al}\right)_{detrital}\right)$$

$$Ba_{bio} = Ba_{total} - (Al \times 0.0029)$$

This approach is accurate at sites where <50% of Ba is aluminosilicate Ba (Dymond et al., 1992). It was assumed that all Al is off aluminosilicate origin, the $(Ba/Al)_{detrital}$ ratio can be estimated independently, the $(Ba/Al)_{detrital}$ ratio remains constant over the studied interval, and the measured Ba signal only consists of biogenic and detrital Ba. We assumed a $(Ba/Al)_{detrital}$ value of 0.0029, as this resulted the lowest positive Ba_{bio} values (a value >0.0029 resulted in negative Ba_{bio} values).

From the measured elemental concentrations, we calculated several other elemental ratios to reconstruct variations in terrestrial input and redox-conditions: Fe/Al, V/Al, and additionally Ti/Al, K/Al, and Mg/Al for validation purposes (supplementary information). Al was used as normalization parameter as it generally behaves conservatively (Calvert & Pedersen, 2007).

3.4 Age model and spectral analysis

Acycle (Li et al., 2019) was used for depth and time series analyses. Depth/time series were sorted, interpolated to uniformly spacing, and detrended to remove long-term trends. Power spectral analysis was performed in the depth/time domain using the multi-taper method (MTM) robust AR(1) model. For statistical significance, 95% confidence levels (CLs) were indicated. Band-pass filtering was applied to isolate specific frequency components present in the depth/time series using the Gauss algorithm. Evolutionary spectral analysis was performed to evaluate changes in spectral power with depth/time. The coherence and phase were calculated between a reference and a series for specific frequencies. The phase in degrees was converted to phase in kyr:

$$Phase\ (kyr) = \frac{period\ (kyr)}{360\ °} \times phase\ (°)$$

For conversion to the time domain, we used an adapted version of the orbitally-tuned age model presented by Wubben et al. (in prep.). Initial age control was based on calcareous nannoplankton, planktic foraminifer and diatom biostratigraphy (Mascle et al., 1996; Norris, 1998b; Raffi, pers. comm.; Shafik et al., 1998; Witkowski, pers. comm.) and isotope stratigraphy.

4 Results

4.1 Description of the records

The data is plotted against depth in Figure 2. Values of $\delta^{13}C$ gradually increase from an average of 0.2‰ in cores 26-25X to 0.5‰ in core 24X to 1.2‰ in cores 23-22X. Values of $\delta^{18}O$ decrease from an average of -1.1‰ in core 26X to -1.6‰ in cores 25-23X and then increase to -1.3‰ in core 22X. MS increases from an average of 5.7E-8 m^3/kg in core 26X to 8.4E-8 m^3/kg in cores 25-22X. $CaCO_3$ values fluctuate between 0 and 60%. Several large and steep decreases of up to 40% are recorded in cores 25-24X. In core 26X, TEX_{86}-SST fluctuates between 26.2 and 30.8°C with an average value of 28.2°C. In cores 25-22X, TEX_{86}-SST fluctuates between 27.1 and 33.0°C with an average value of 30.0°C. The highest SST of 33.0°C is reached at 221.05 rmbsf and the lowest SSTs are recorded in core 26X. The BIT index varies between 0.0 and 0.5. Out of the 477 measurements, 24 values are above 0.3 and 7 values are above 0.4. All values >0.4 occur in core 25X and are indicated in the TEX_{86}-SST record (Figure 2). The other calculated GDGT ratios do not suggest TEX_{86} is affected by nonthermal processes (supplementary information).

Ba_{bio} varies between 29 and 2103 ppm and the record is characterized by large peaks with significantly lower peaks in between. These large peaks reach >850 ppm in cores 26-24X. Peaks in lower-resolution part of the record (23-22X) are less defined, possibly due to the lower sampling resolution in this interval. The Ba_{bio} peaks correspond to darker layers seen on the core photos (Figure 2). The Fe/Al and V/Al records resemble the Ba_{bio} record, with clear peaks corresponding to large Ba_{bio} peaks and smaller peaks in between. Records of Ti/Al, K/Al and Mg/Al display similar patterns (supplementary information). Fe/Al varies between 0.33 and 1.22 ppm and V/Al between 0.0011 and 0.0030 ppm.

From ~260 rmbsf, the lithology gradually darkens and then sharply switches back to light grey at ~257 rmbsf. Between ~259 and ~257 rmbsf, $\delta^{13}C$ decreases by 1.31‰, $\delta^{18}O$ decreases by 1.11‰, and TEX_{86}-SST increases by 5.1°C. From ~260 rmbsf, MS decreases and then gradually increases to reach its average of 8.4E-8 m^3/kg from 256.9 rmbsf. $CaCO_3$ decreases to 3% at 257.7 rmbsf and then increases sharply to 51% at 257.1 rmbsf. Two Ba_{bio}

peaks of >1000 ppm occur between ~260 and ~257 rmbsf. The first peak concurs with high values of Fe/Al and V/Al and the second peak concurs with the second-highest Fe/Al peak of the whole interval and with high V/Al.

Regular alternations of ~10, ~2.5-3, ~1.5-2 and ~0.5-1 m are recognized between ~258-218 rmbsf (cores 25-22X). Between ~268-258 rmbsf (core 26X), 4 m variations are observed instead of ~2.5-3 m variations. Generally, minima of $\delta^{13}C$ and $\delta^{18}O$ correspond to maxima of $CaCO_3$ and TEX_{86}-SST and minima of Ba_{bio}. Stronger minima, occur every ~2.5-3 m for $\delta^{18}O$ and every ~2.5-3 and ~10 m for $\delta^{13}C$ and correspond to increased amplitudes of small-scale fluctuations. In the TEX_{86}-SST record, bundles of relatively high SST peaks occur every ~2.5-3 m and are separated by lower SST peaks and more pronounced SST minima. These bundles are asymmetrical in core 26X and relatively symmetrical in cores 25-22X. Deviations from this bundling pattern are observed in the intervals ~258-243 rmbsf and ~237-232 rmbsf. In core 25X, pronounced SST minima occur every ~1.5-2 m and concur with BIT index minima. The pronounced Ba_{bio} peaks in cores 25-24X occur regularly every ~1.5-2 m and are separated by two or three ~0.5-1 m fluctuations with significantly lower amplitude. They concur with pronounced TEX_{86}-SST and $CaCO_3$ minima. Intervals with lower amplitude variation are recognized from ~248-246 rmbsf in the MS record and from ~238-233 rmbsf in the $\delta^{13}C$, $\delta^{18}O$ and MS records, which overlap with intervals in the TEX_{86}-SST record with deviating bundling patterns. Highest variation in the $\delta^{13}C$ and $\delta^{18}O$ records is seen in cores 26, 25 and 22X.

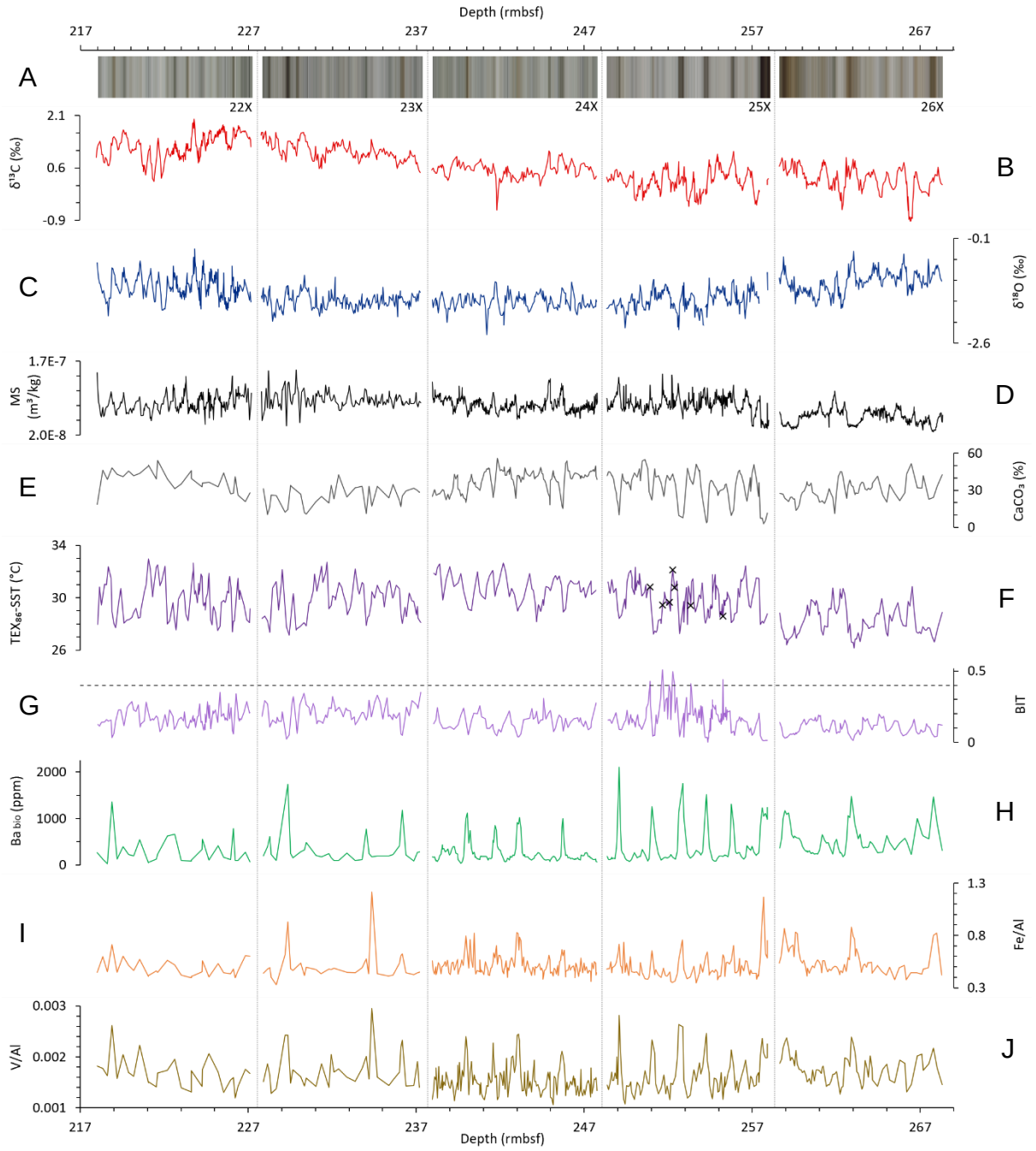

Figure 2. ODP Site 959 records of core colour (A), bulk carbonate $\delta^{13}C$ (B), $\delta^{18}O$ (C), MS (D), wt% $CaCO_3$ (E), TEX_{86}-SST (F), BIT (G), Ba_{bio} (H), Fe/Al (I) and V/Al (J) plotted against depth. The colour record is derived from core photos (Wubben et al., in prep.). The records span from ~268 to ~218 rmbsf corresponding to cores 26-22X. F: TEX_{86}-SST values with a BIT index >0.4 are marked by black crosses. G: the BIT threshold of 0.4 is indicated by the dashed black line.

4.2 Spectral analysis and bandpass filtering in the depth domain

Spectral analysis in the depth domain is in line with the visual observations and reveals four frequency bands in which significant spectral power is regularly found: 0.085-0.12 m^{-1}, 0.22-0.5 m^{-1}, 0.5-0.65 m^{-1} and 0.85-2.1 m^{-1}, corresponding to periods of 11.8-8.3 m, 4.5-2 m, 2-1.5 m and 1.2-0.5 m, respectively (Figure 3). Significant spectral power in the 0.85-2.1 m^{-1} (2-1.5 m) band is present in all depth series. Power in the 0.085-0.12 m^{-1} (11.8-8.3 m) band reaches only above the 95% CL in the spectrum of $\delta^{13}C$. Power in the 0.22-0.5 m^{-1} (4.5-2 m) band is strong in spectra of $\delta^{13}C$, $\delta^{18}O$, TEX_{86}-SST, Fe/Al and V/Al. The spectrum of Ba_{bio} is dominated by power in the 0.5-0.65 m^{-1} (2-1.5 m) band, which is also strongly present in spectra of Fe/Al and V/Al.

Bandpass filtering of $\delta^{13}C$ and TEX_{86}-SST shows good correspondence in terms of pacing and amplitude modulation between ~0.5, ~2.5 and ~10 m cycles (Figure 4). Higher amplitudes of the ~0.5 m cycle mostly occur during ~2.5 m $\delta^{13}C$ minima and ~2.5 m TEX_{86}-SST maxima. Amplitude modulation of the ~2.5 m cycles approximately follows the ~10 m cycle, with highest amplitudes corresponding to ~10 m $\delta^{13}C$ minima and ~10 m TEX_{86}-SST maxima. In the lower interval (~258-248 rmbsf), the ~10 m filter is slightly displaced from the peak of amplitude modulation at ~254 rmbsf. Usually, one ~10 m cycle contains four ~2.5 m cycles and one ~2.5 m cycle contains four or five ~0.5 m cycles. The ~1.5 m cycle in the Ba_{bio} series follows the large Ba_{bio} peaks, while the ~0.5 m cycle also follows the lower-amplitude fluctuations and correlates with ~0.5 m cycles in the $\delta^{13}C$ and TEX_{86}-SST series (Ba_{bio} maxima correlate with $\delta^{13}C$ maxima and TEX_{86}-SST minima) . One ~1.5 m cycle consists of two or three ~0.5 m cycles.

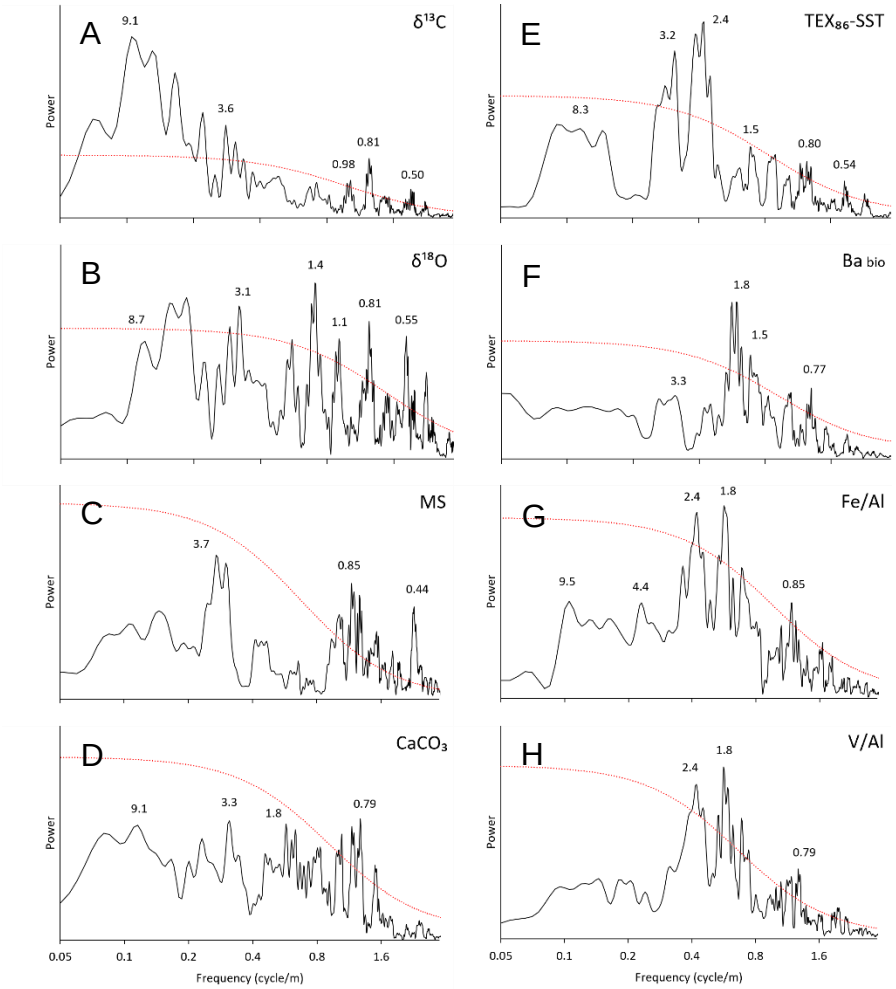

Figure 3. Power spectral analysis (MTM) in the depth domain of $\delta^{13}C$ (A), $\delta^{18}O$ (B), MS (C), wt% $CaCO_3$ (D), TEX_{86}-SST (E), Ba_{bio} (F), Fe/Al (G) and V/Al (H) (black). The 95% CL is indicated in red. The numbers indicate the periods (in m) of specific peaks.

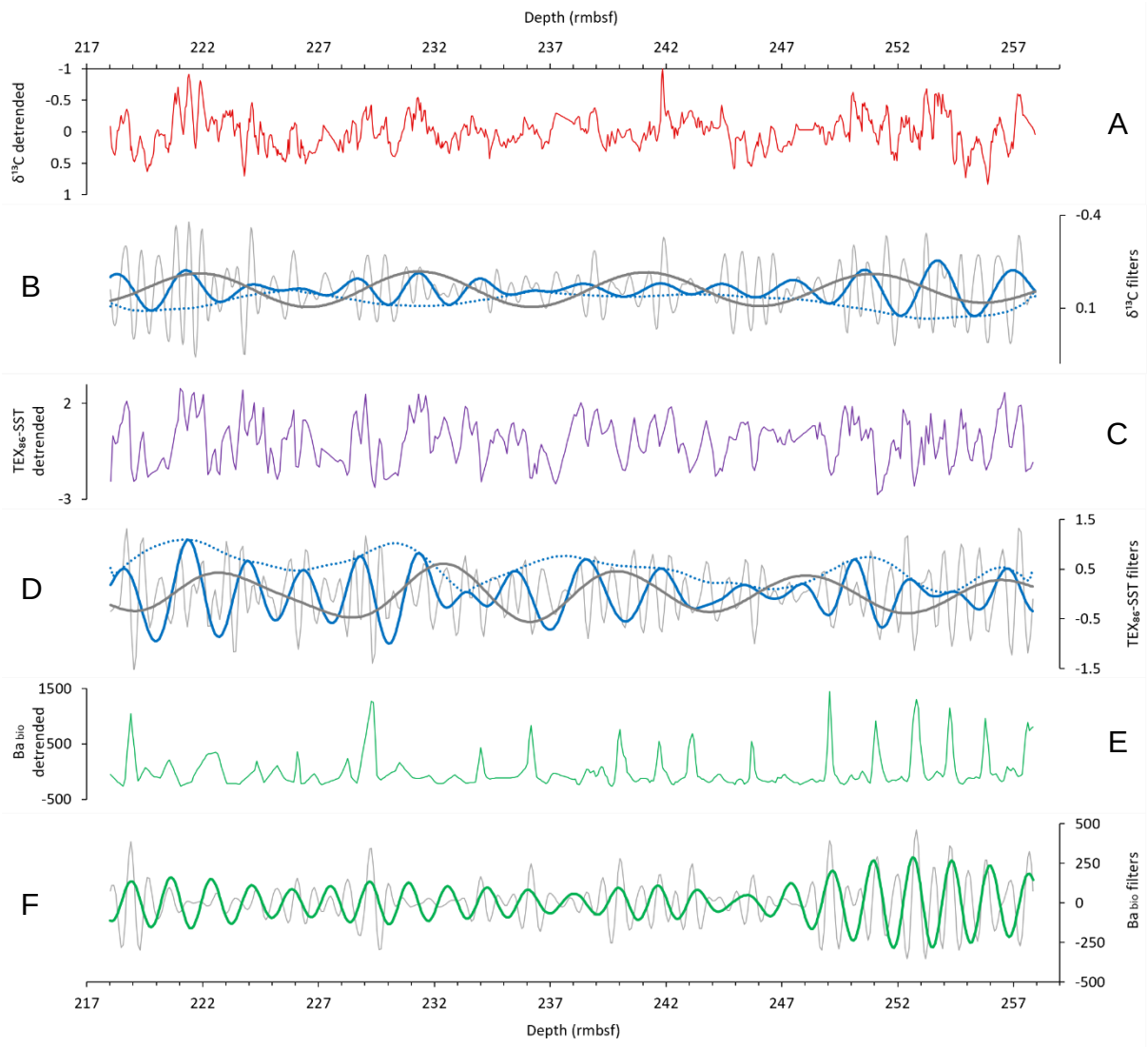

Figure 4. Bandpass filtering of ~0.5 m (light grey), ~2.5 m (blue) and ~10 m (dark grey) cycles for $\delta^{13}C$ (B), TEX_{86}-SST (D) and Ba_{bio} (F) depth series in the interval ~258-~218 rmbsf (cores 25-22X) compared to the interpolated and detrended series (A, C, E). $\delta^{13}C$ and TEX_{86}-SST were detrended using the LOWESS method and Ba_{bio} was demeaned. $\delta^{13}C$ was filtered at frequencies of 0.9-2.1, 0.26-0.415 and 0.085-0.12 m^{-1}, TEX_{86}-SST at 0.937-2.02, 0.22-0.5 and 0.065-0.18 m^{-1}, and Ba_{bio} at 0.93-1.71 and 0.5-0.65 m^{-1}. Blue dotted series indicate amplitude modulation of the $\delta^{13}C$ 0.26-0.415 m^{-1} and TEX_{86}-SST 0.22-0.5 m^{-1} filters.

5 Age model and analyses in the time domain

5.1 Age model

Based on cycle ratios, amplitude modulation and the initial biostratigraphic age model, power in the 0.085-0.12 m^{-1} (11.8-8.3), 0.22-0.5 m^{-1} (4.5-2 m) and 0.85-2.1 m^{-1} (1.2-0.5 m) bands is linked to 400-kyr eccentricity, 100-kyr eccentricity and precession, respectively. ~10 m and ~2.5 m $\delta^{13}C$ minima are linked to eccentricity maxima, in agreement with amplitude modulation of $\delta^{13}C$ and TEX_{86}-SST bandpass filters.

The age model is based on that of Wubben et al. (in prep.), in which eccentricity related $\delta^{13}C$ minima were linked to the orbital solution using isotope- and biostratigraphy. In the age

model, ~100 kyr is missing either between cores 22 and 23X or between cores 23 and 24X. In contrast to Wubben et al. (in prep.), we assume ~100 kyr is missing between cores 22 and 23X because in this option the two weaker 100-kyr eccentricity maxima at ~16.2 and 16.3 Ma correlate well with the ~233-237 rmbsf interval of decreased variability of $\delta^{13}C$, $\delta^{18}O$ and MS and the less distinct bundling pattern of TEX_{86}-SST.

Tuning of the ~258-218 rmbsf interval corresponds well with the available bioevents and the observed isotope events at ~221 and ~258 rmbsf related to the ~15.6 Ma hyperthermal event and MCO onset (~17 Ma), respectively (Figure 5). Tuning of the lower interval (~258-268 rmbsf) results in ages that are >0.5 Ma younger than suggested by the bioevents. Possibly a larger hiatus is present at ~258 rmbsf. We consider the age scale in this interval as a floating tuning, in which tie-points can be displaced to older 100 kyr eccentricity maxima.

Conversion of the depth series to time results in a resolution of ~1 kyr for MS (except ~3 kyr in core 23X), ~2 kyr for $\delta^{13}C$ and $\delta^{18}O$, ~3 kyr for TEX_{86}-SST, and for the elemental records (Ba_{bio}, Fe/Al, V/Al) ~3 kyr in the high-resolution part (26-24X) and ~13 kyr in the low-resolution part (23-22X).

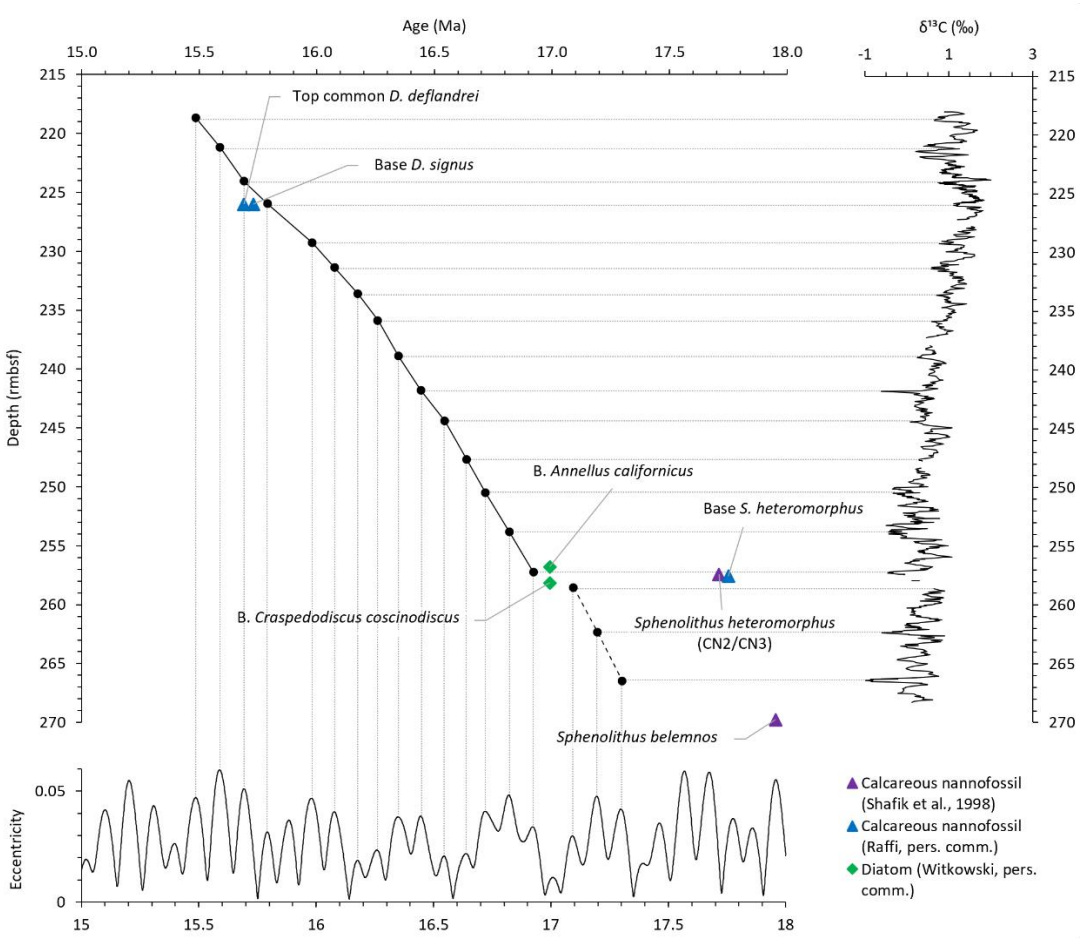

Figure 5. Correlation between $\delta^{13}C$ and eccentricity (La2004) and the resulting age-depth model (black) with positions of calcareous nannofossil and diatom bioevents. Age model for the ~15.4-17 Ma interval (black line) and floating age scale for the ~17-17.4 Ma interval (dashed black line).

5.2 Spectral analysis and bandpass filtering in the time domain

The orbitally-tuned time series display significant power in the period ranges ~19-24 kyr, ~40-70 kyr and ~87-134 kyr (Figure 6). All time series display high spectral power for periods of ~19-24 kyr. Power is divided in peaks at ~19-20 kyr, ~23-24 kyr, and in some cases also ~21 kyr. This corresponds well with periods of precession (19, 22, 23 kyr). Other communal high-frequency peaks are observed at ~16 kyr and ~30 kyr. Spectra of $\delta^{18}O$, $CaCO_3$, TEX_{86}-SST, Ba_{bio}, Fe/Al and V/Al show significant power in the ~40-70 kyr band. Although some peaks correspond to the period of obliquity (41 kyr), most power is located around a period of ~50 kyr. In the ~87-134 kyr band, high power is present in spectra of $\delta^{13}C$, $\delta^{18}O$, MS, $CaCO_3$, TEX_{86}-SST, Fe/Al and V/Al and corresponds well with the periods of short eccentricity (90, 95, 100, 106, 115, 124, 132 kyr). Power around these periods is very low in the spectrum of Ba_{bio}. For periods >150 kyr, high spectral power is found around ~150 and ~167 kyr in the spectrum of $\delta^{18}O$ and around ~223, ~282, ~367 and ~525 kyr in the spectrum of $\delta^{13}C$. The periods of ~367 and ~525 correspond with periods of long eccentricity (~334, ~417, ~527 kyr).

Bandpass filtering (Figure 7) shows that the filtered ~100 kyr cycle of $\delta^{13}C$ and TEX_{86}-SST corresponds well with the solution of eccentricity, in terms of ~100 kyr pacing and ~400 kyr amplitude modulation. The ~367 kyr $\delta^{13}C$ filter corresponds well with long eccentricity. Bandpass filtering and evolutionary spectral analysis of TEX_{86}-SST (Figure 8) show that the highest amplitudes of the ~40-50 kyr cycle occur during intervals with lower variance of eccentricity (~400 kyr and ~2.4 Myr minima), where the bundling pattern is less well expressed. This pattern of amplitude modulation does not correspond to that of the filtered ~40-60 kyr Ba_{bio} cycle, except around ~16.8 Ma. The ~40-50 kyr TEX_{86}-SST cycle and ~40-60 kyr Ba_{bio} cycle are generally out of phase, but the TEX_{86}-SST filter picks up an additional cycle around ~16.71, ~16.06, ~15.67 and ~15.59 Ma. The ~40-50/~40-60 kyr cycle is approximately in phase with ~19-24 kyr cycle, with mostly two and sometimes three ~19-24 kyr cycles within one ~40-50/~40-60 kyr cycle.

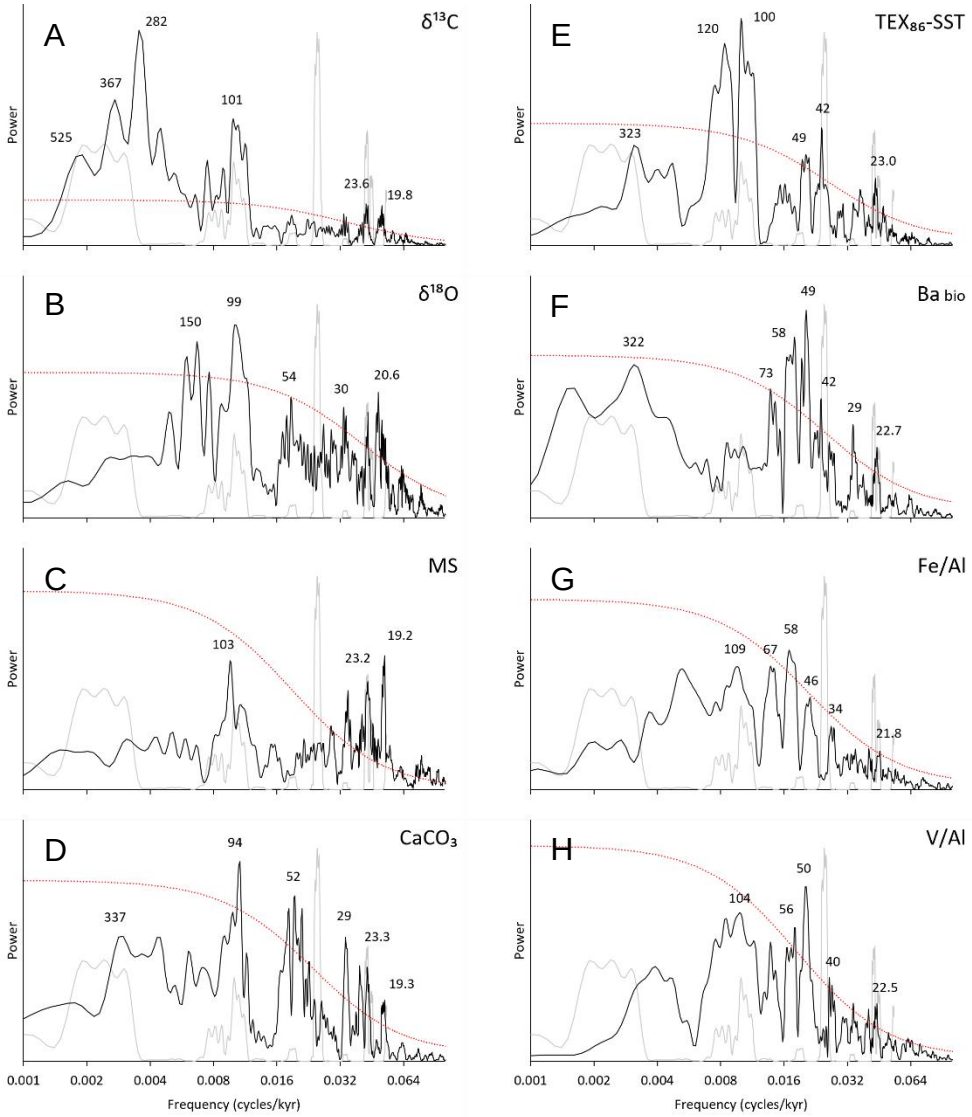

Figure 6. Power spectral analysis (MTM) in the time domain of $\delta^{13}C$ (A), $\delta^{18}O$ (B), MS (C), wt% $CaCO_3$ (D), TEX_{86}-SST (E), Ba_{bio} (F), Fe/Al (G) and V/Al (H) (black) in the time domain for the interval ~16.9-15.4 Ma (cores 25-22X). The 95% CL is indicated in red. The numbers indicate the periods (in kyr) of specific peaks. For comparison, the spectrum of the sum of normalized eccentricity, tilt and precession (ETP) (La2004) is plotted in light grey.

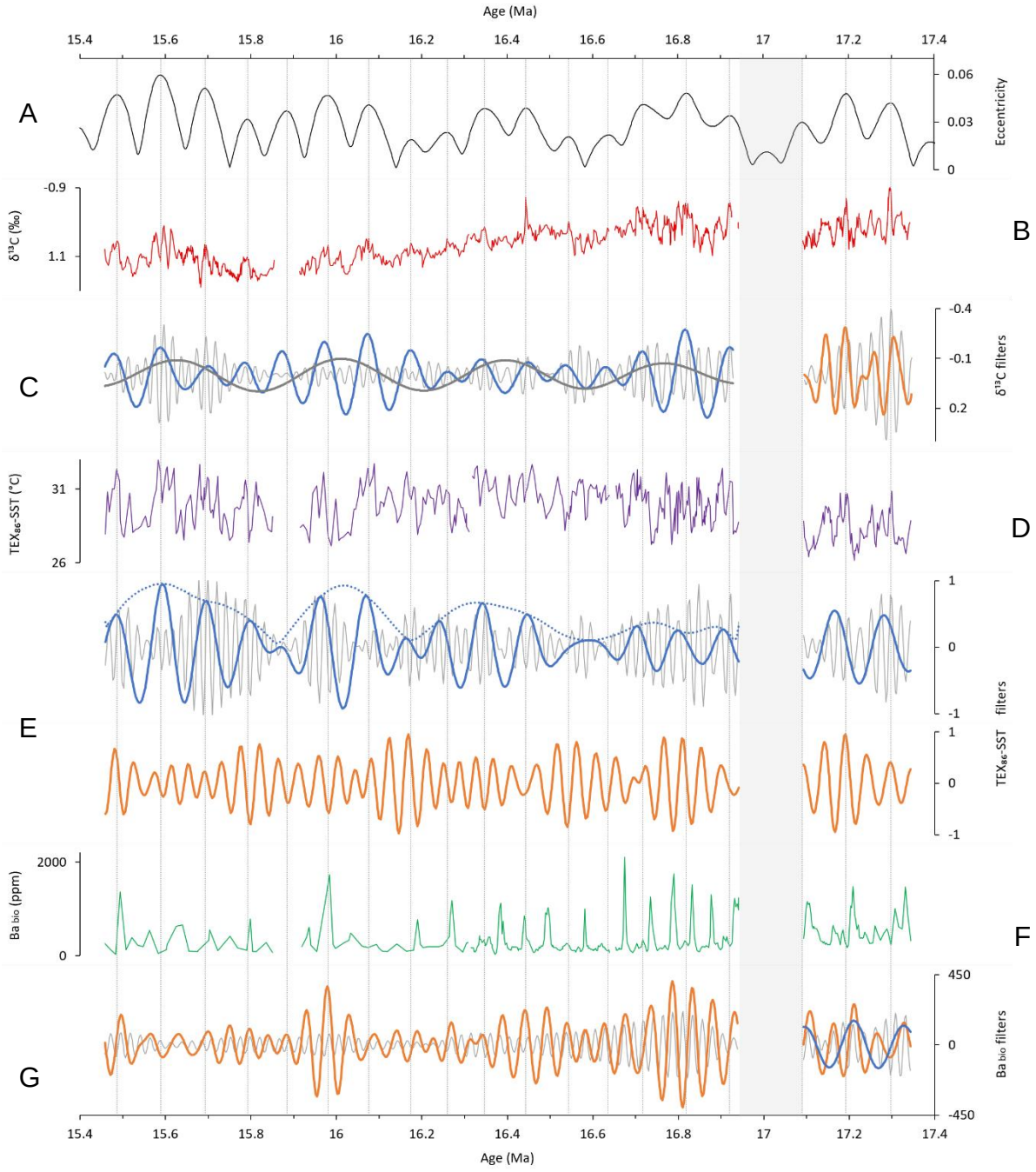

Figure 7. Bandpass filtering of ~19-24 kyr (light grey), ~40-70 kyr (orange), ~87-134 kyr (blue) and ~367 kyr (dark grey) cycles for $\delta^{13}C$ (C), TEX_{86}-SST (E) and Ba_{bio} (G) time series in the intervals ~17.4-17.1 Ma and ~16.9-15.4 Ma. For comparison, the solution of eccentricity (La2004) (A) and the $\delta^{13}C$, TEX_{86}-SST and Ba_{bio} time series are plotted (B, D, F). For the ~17.4-17.1 Ma interval, $\delta^{13}C$ was linearly detrended and TEX_{86}-SST and Ba_{bio} were demeaned. $\delta^{13}C$ was filtered at frequencies of 0.035-0.05 and 0.01-0.028 kyr^{-1}, TEX_{86}-SST at 0.038-0.05 and 0.007-0.011 kyr^{-1}, and Ba_{bio} at 0.038-0.05, 0.012-0.025 and 0.0065-0.01 kyr^{-1}. For the interval ~16.9-15.4 Ma, $\delta^{13}C$ and TEX_{86}-SST were detrended using the LOWESS method and Ba_{bio} was demeaned. $\delta^{13}C$ was filtered at frequencies of 0.0381-0.0531, 0.069-0.0125 and 0.00218-0.00313 kyr^{-1}, TEX_{86}-SST at 0.0391-0.0553, 0.0185-0.027 and 0.00619-0.01235 kyr^{-1}, and Ba_{bio} at 0.041-0.047 and 0.0158-0.025 kyr^{-1}. Blue dotted series indicate amplitude modulation of the TEX_{86}-SST 0.00619-0.01235 kyr^{-1} filter.

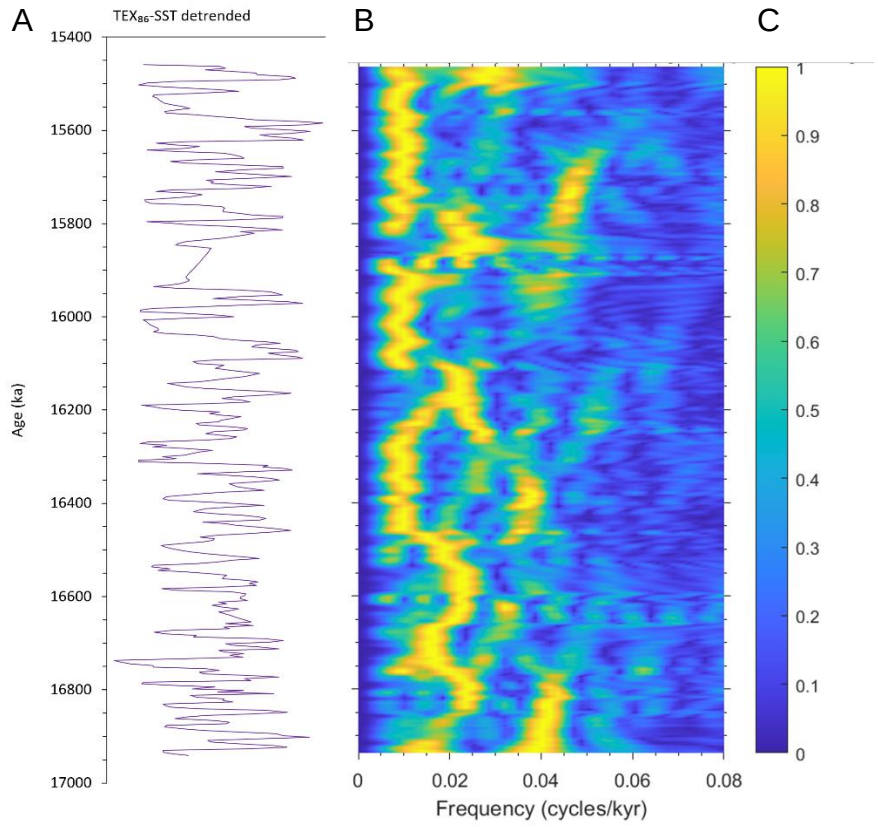

Figure 8. Evolutionary spectral analysis (Fast Fourier transform, LAH) of TEX_{86}-SST time series (B) in the interval ~17-15.4 Ma. TEX_{86}-SST was detrended using the LOWESS method (A). A sliding window of 150 kyr and step size of ~3.5 kyr was used. The degree of power is indicated by the colour scale (C).

5.3 Origin of the ~50 kyr cycle

Spectral analysis between ~17 and ~15.4 Ma shows that high spectral power is present around ~50 kyr, and sometimes also around ~40 or ~60-70 kyr in series of Ba_{bio}, Fe/Al, V/Al, TEX_{86}-SST and $CaCO_3$ (Figure 6). Bandpass filtering shows that this cycle follows the pronounced Ba_{bio}, Fe/Al, and V/Al peaks and minima of TEX_{86}-SST and $CaCO_3$ (Figure 7). Bandpass filters of the ~40-60 kyr cycle and ~100 kyr eccentricity-related cycle do not show a clear correlation, suggesting that the ~50 kyr cycle is not related to half a short eccentricity cycle. Obliquity has a period of ~41 kyr, but its spectrum also shows power around ~29 kyr and ~51-54 kyr. However, these cycles are very weak and cannot explain the presence of a strong ~50 kyr cycle in our records.

In the high-resolution part between ~17 and ~16.3 Ma, bandpass filtering of Ba_{bio} reveals that maxima of the ~40-60 kyr cycle correspond to every second, and sometimes every third, precession-related cycle (Figure 7). Thus, it seems that Ba_{bio} peaks are paced by precession but amplified every second or third cycle. This pattern is similar to interference between astronomical solutions of precession and obliquity, with a ratio close to 2:1. Summer insolation is increased during obliquity maxima and decreased during obliquity minima. At latitudes where both precession and obliquity influence insolation, obliquity enhances or reduces the insolation maxima and minima caused by precession. As the ratio between solutions of

precession and obliquity is not exactly 2:1, the interference pattern is not perfect and obliquity sometimes enhances the third next precession cycle instead of the second. Bandpass filtering and evolutionary spectral analysis of TEX_{86}-SST support this hypothesis, as they reveal that the ~40-60 kyr cycle is mainly present within ~400 kyr and ~2.4 Myr eccentricity minima. Within these minima, the amplitude of the ~100 kyr eccentricity cycle is reduced and obliquity becomes relatively more important.

As the solutions of precession consists of components of ~23.5, ~22 and ~19 kyr, two cycles span ~38-47 kyr and three cycles span ~57-69 kyr. Power of the ~19 kyr component is weak during ~2.4 Myr eccentricity minima, making two precession cycles ~44-47 kyr and three 66-69 kyr. From ~16.9 to ~16.3 Ma, durations between large Ba_{bio} peaks are approximately 58, 45, 42, 56, 59, 93, 87, 56 and 54 kyr (Figure 7). The ~40-60 kyr filter picks up an additional cycle between the peaks spanning 93 and 87 kyr. This means that the total duration of 550 kyr corresponds to 11 cycles, resulting in an average of 50 kyr per cycle. The average in the interval ~16.9-16.7 Ma is 52 kyr and the average in the interval ~16.7-16.3 is 48 kyr. Thus, spectral power around 50 kyr is present because this period gives in the best fit with the large Ba_{bio} peaks.

In total, the 550 kyr interval spans 23 or 24 precession cycles according to bandpass filtering of $\delta^{13}C$, TEX_{86}-SST and Ba_{bio} (Figure 7). This results in an average of ~24 or ~23 kyr per precession cycle, which is approximately in line with the expected period of precession in this interval. However, some intervals that include 2 precession cycles are 54-58 kyr, which results in precession cycles of 27-29 kyr on average. One interval of 59 kyr spans 3 precession cycles, resulting in an average of 19.7 kyr per cycle. These periods are longer or shorter than expected. The discrepancies might be the result of distortion and/or slightly incorrect positions of some tie-points used in the age model. The tie-points are based on the positions of pronounced $\delta^{13}C$ minima, which are linked to ~100 kyr eccentricity maxima. Their actual position might be slightly displaced from eccentricity maxima as it depends also on precession.

In conclusion, the ~50 kyr cycle originates from interference between precession and obliquity during which every second, and sometimes third, precession cycle is amplified by obliquity.

5.4 Phase relations

Coherence and phase were calculated for periods of ~23 and ~44 kyr in the interval 16.65-16.93 Ma (core 25X) using $CaCO_3$ multiplied by -1 as reference series (Table 1). Also, the TEX_{86}-SST series was multiplied by -1. In this way, maxima of -$CaCO_3$ correspond to maxima of -TEX_{86}-SST, $\delta^{13}C$, $\delta^{18}O$, MS, Ba_{bio}, Fe/Al and V/Al.

At the ~23 kyr period, $\delta^{18}O$ and -TEX_{86}-SST are approximately in phase and lead -$CaCO_3$ by ~4.6 kyr. Also, $\delta^{13}C$ and Ba_{bio} are approximately in phase and lead -$CaCO_3$ by ~2.5 kyr. Fe/Al leads -$CaCO_3$ by 2.0 kyr. V/Al is approximately in phase with -$CaCO_3$ and leads by just 0.2 kyr. MS lags -$CaCO_3$ by 2.9 kyr. At the ~44 kyr period, $\delta^{18}O$ significantly leads -$CaCO_3$ (by 14.2 kyr) and the other series. TEX_{86}-SST leads -$CaCO_3$ by 0.7 kyr and Ba_{bio} and Fe/Al are approximately in phase with a lead of ~0.4 kyr. V/Al lags -$CaCO_3$ by 3.6 kyr. Phases of $\delta^{13}C$ and MS are left out as these series do not show significant power around a period ~44 kyr.

Table 1. Coherency and phase relative to -$CaCO_3$ at a period of 23.4 kyr and 43.8 kyr for the interval ~16.93-16.65 Ma (core 25X).

	23.4 kyr			**43.8 kyr**		
	Coherency	*Phase (°)*	*Phase (kyr)*	*Coherency*	*Phase (°)*	*Phase (kyr)*
$\delta^{18}O$	0.92	71.6	4.7	0.90	116.3	14.2
-TEX_{86}-SST	0.83	68.8	4.5	0.95	5.5	0.7
$\delta^{13}C$	0.93	38.8	2.5	N.A.		
Ba_{bio}	0.84	36.5	2.4	0.97	3.6	0.4
Fe/Al	0.69	31.4	2.0	0.99	2.8	0.3
V/Al	0.84	2.6	0.2	0.95	-29.6	-3.6
MS	0.72	-45.1	-2.9	N.A.		

6 Interpretation and comparison of proxy records

6.1 TEX_{86}-SST

Annual SST at Site 959 was highly variable during the Early/Middle Miocene. Modern SST around Site 959 varies between ~25°C in summer when upwelling occurs and ~29°C in winter with an annual mean of ~28°C (Djakouré et al., 2017). Before ~17 Ma, TEX_{86}-derived SST fluctuates between 26.2-30.8°C with an average of 28.2°C, close to the modern annual mean SST. Pronounced minima are up to 2°C colder than the modern annual mean, but warmer than modern summer upwelling SST. Pronounced maxima are up to 3°C warmer than modern annual mean SST and up to 2°C warmer than modern non-upwelling winter SST. After ~17 Ma, SST fluctuates between 27.1-33.0°C with an average of 30.0°C, 2°C warmer than the modern annual mean SST. Temperatures of pronounced SST minima are close to the modern annual mean SST, while pronounced SST maxima are 2-5°C warmer than the modern annual mean.

MCO (~17-15 Ma) SSTs at Site 959 are comparable to those obtained for the Indo-Pacific and mid-latitude North Atlantic. During the MCO (~17-15 Ma), Mg/Ca-derived SST in the Indo-Pacific region varied between ~27 and ~31.5°C, with an average around ~29.5°C (Sosdian & Lear, 2020). This is very similar to TEX_{86}-SSTs at Site 959, except for maximum temperatures which are ~1.5°C higher at Site 959. Sosdian & Lear (2020) suggested a tropics-wide response to changes in greenhouse gas forcing, AIS dynamics and high-latitude temperature. In the Indo-Pacific, SSTs were warm during periods of high pCO_2, high sea level and warm deep waters (and vice versa) (Sosdian & Lear, 2020). The Indo-Pacific and Site 959 SST records display similarities, however, the resolution differs too much for good comparison. Like Site 959 TEX_{86}-SST, mid-latitude North Atlantic TEX_{86}-SST varied between ~27 and ~33°C during the MCO (~17-15 Ma) (Super et al., 2020). Although resolution is relatively low, North Atlantic (mid- and high-latitude) SSTs display an overall decreasing trend during the MCO (Super et al., 2020), which is not seen in the Site 959 SST record. Additionally, pre-MCO (~18.5-17 Ma) North Atlantic SSTs are relatively high compared to those during the MCO (Super et al., 2020), in contrast to Site 959 pre-MCO SST which was on average ~2°C colder than MCO SST. These differences suggest that the North Atlantic was likely influenced by different processes or water masses compared to Site 959. Between ~15 and 11 Ma, Site 959 TEX_{86}-SST fluctuated around an average of ~29°C (Van Der Weijst, 2021 preprint), only 1°C lower compared to the MCO. Thus, SST at Site 959 remained relatively stable between ~17 and ~11 Ma.

At Site 959, TEX_{86} mainly represents (sub)surface temperatures as GDGT-2/3 values are below 5 in most on the studied interval. TEX_{86} values vary between 0.66 and 0.83 (on average 0.74), indicating that the type of calibration (linear or non-linear) affects reconstructed SSTs in the upper range (Sluijs et al., 2020). TEX_{86}-SSTs might not completely represent annual SST as TEX_{86} might be biased towards the season with the highest export production (Sluijs et al., 2020).

6.2 Fe/Al

Terrigenous elements (e.g. Fe, Ti, K, Mg) can be transported to marine sediments through aeolian or fluvial processes and both may result in similar elemental ratios measured in the sediment (Martinez-Ruiz et al., 2015). The BIT index was generally low and pronounced peaks of Fe/Al concurred with BIT minima, indicating that fluvial processes were not responsible for the increased input of Fe. The Fe/K ratio is commonly used as a proxy for soil weathering and humidity, as strongly weathered soils in tropical humid regions are generally enriched in Fe and Al (Govin et al., 2012). However, Saharan dust also contains Fe (Moskowitz et al., 2016) and Bozzano et al. (2002) used Fe/Al as indicator of Saharan and Sahelian dust input off northwest Africa. Dust input is a more logical reason for increased Fe/Al at Site 959 as fluvial input was low and both Fe and Al are enriched in strongly weathered soils (cancelling each other out). This interpretation is supported by records of Ti/Al, K/Al and Mg/Al, which show similar trends as the Fe/Al record (supplementary information). The Ti/Al ratio has often been used as a proxy for aeolian input and sediment grain-size (Akinnigbagbe et al., 2018; Beckmann et al., 2005; Calvert & Pedersen, 2007; Govin et al., 2012; Martinez-Ruiz et al., 2015; Vallé et al., 2017). Ti in aeolian dust mainly resides in heavy minerals, which are transported along with coarser quartz grains (Calvert & Pedersen, 2007; Martinez-Ruiz et al., 2015). Both K and Mg are enriched in sand dunes and arenosols in (semi-)arid regions with very low weathering in the Sahara and Sahel (Govin et al., 2012). Although K/Al and Mg/Al are often used as indicators of fluvial input (Calvert & Pedersen, 2007; Martinez-Ruiz et al., 2015), they more likely represent variations in dust input at Site 959.

North Africa holds a large dust source, including the most intense source located in Chad (Lake Chad Basin and Bodélé depression) which is active all year long (Prospero et al., 2002). Ti, Fe, K, and Mg are all present in Saharan mineral dust (Linke et al., 2006) and NE trade winds transport dust from central North Africa (Chad) to the eastern equatorial Atlantic during winter (Prospero et al., 2002; Stuut et al., 2005). Aridification of North Africa occurred from the Early Miocene (Hounslow et al., 2017; Zhang et al., 2014). Based on climate simulations, the Early Miocene North African climate was mainly semiarid with restricted arid areas (Zhang et al., 2014). Beckmann et al. (2005) assigned the desert areas of the proto-Kalahari in southern Africa as dust source at Site 959 in the Cretaceous. However, in the Upper Cretaceous (~80 Ma), the African continent was displaced to the south compared to the present and Miocene, with the equator located over the North African continent and Site 959 located at ~10°S (Beckmann et al., 2005; Van Hinsbergen et al., 2015). At present, only two small dust sources are present in southern Africa in July (Etosha pan and Makgadikgadi depression and pan) (Prospero et al., 2002). During the Miocene, dust deposited at Site 959 seems more likely to have originated from North Africa rather than southern Africa as the continental configuration was more similar to the present than the Cretaceous. We thus interpret increased Fe/Al at Site 959 as increased dust input from North Africa, transported by NE trade winds during winter.

6.3 Ba_{bio}

Ba_{bio} is used to reconstruct past variations in ocean productivity, as it is strongly linked with export productivity (Dymond et al., 1992; Gingele & Dahmke, 1994; Kasten et al., 2001; Piela et al., 2012; Rutsch et al., 1995). Barite is the main carrier of particulate barium and forms in supersaturated microenvironments after the release of Ba during plankton decomposition (Ganeshram et al., 2003). Ba_{bio} has an average burial flux of 30%, which is higher than other biogenic components (Dymond et al., 1992). Remobilization and diagenetic redistribution of barite can occur in anoxic sediments where sulphate reduction is common (Dymond et al., 1992; Gingele & Dahmke, 1994). The biogenic Ba fraction was estimated using a $(Ba/Al)_{detrital}$ ratio of 0.0029. Although this value is lower than the 0.005-0.01 range based on the average crustal composition and values of 0.0045 determined for the Ceará Rise (Kasten et al., 2001) and the continental slope of the Congo Fan (Rutsch et al., 1995), it falls within the range of values obtained directly by sequential extraction for various sites in the Atlantic (0.0014-0.0041) (Reitz et al., 2004).

Decomposition of organic matter at the seafloor can reduce oxygen concentrations. V is a redox-sensitive element and can be used to reconstruct past redox conditions. V is sensitive to minor changes in oxygen concentration and starts to accumulate as oxyhydroxides under dysoxic to suboxic conditions, in the absence of oxygen and sulfide (Calvert & Pedersen, 2007; Martinez-Ruiz et al., 2015).

7 Discussion

7.1 Global monsoon perspective

On a global scale, monsoon dynamics affect weathering rates and nutrient supply, and thereby the oceanic carbon reservoir and $\delta^{13}C$ (Ma et al., 2011; Wang, 2009). Orbital-scale monsoon variability is dominated by precession which is modulated by eccentricity. In contrast to precession, the response to eccentricity is in phase between the northern and southern hemisphere. ~400 kyr long eccentricity cycles were recognized in various $\delta^{13}C$ records from the Cenozoic (e.g. Cramer et al., 2003; Holbourn et al., 2007; Liebrand et al., 2016) and from the Cretaceous (Giorgioni et al., 2012), under both greenhouse and icehouse conditions. The relatively strong ~400 kyr $\delta^{13}C$ cycle probably originates from the long residence time of carbon in the oceanic reservoir (>100 kyr) (Wang, 2009).

The bulk carbonate $\delta^{13}C$ record of Site 959 is strongly imprinted by ~400 kyr and ~100 kyr eccentricity, which modulate the precession-scale variations. Minima of $\delta^{13}C$ correspond to eccentricity maxima, in agreement with other tuned $\delta^{13}C$ records (e.g. Holbourn et al., 2007; Liebrand et al., 2016) and modelling simulations (Ma et al., 2011). Bulk carbonate $\delta^{13}C$ can be influenced by both surface and deep water processes, but it is shown that both surface and deep water $\delta^{13}C$ co-vary at the ~400 kyr cycle (Ma et al., 2011).

The MCO part (~16.9-15.4 Ma) of the Site 959 $\delta^{13}C$ record starts just after carbon-isotope maximum 1 (CM1) and ends at CM4a (Holbourn et al., 2007; Woodruff & Savin, 1991), spanning approximately four ~400 kyr cycles.

Prominent ~400 and ~100 kyr variability is also observed in Early Miocene records of $CaCO_3$ and benthic foraminiferal $\delta^{13}C$ and $\delta^{18}O$ from Walvis Ridge (southeastern Atlantic Ocean) (Liebrand et al., 2016) and MCO records of carbonate dissolution and benthic foraminiferal $\delta^{13}C$ from the Pacific (Holbourn et al., 2007).

7.2 Regional monsoon

Regionally, the response of the monsoon to astronomical insolation forcing and its effect on the local climate depends on the regional setting. In North Africa, the regional monsoon affected sea surface temperature, dust input and productivity.

Overall, the sedimentary records of Site 959 show that the regional climate was paced by precession, obliquity and eccentricity during the Early/Middle Miocene (~17.4-15.4 Ma). Although, the response to astronomical insolation forcing varied between proxies and through time. Three phases with distinct climate variability were observed: (1) asymmetrical ~100 kyr variability before the MCO (~17.4-17 Ma), (2) strong obliquity forcing at the beginning of the MCO (~17-16.5 Ma) during a ~2.4 Myr eccentricity minimum, and (3) symmetrical ~100 kyr variability and ~400 kyr modulation in the later part of the MCO (~16.5-15.4 Ma) (Figure 7).

Pronounced SST minima occurred during eccentricity minima while the highest SSTs occurred during eccentricity maxima in response to an enhanced seasonal contrast. Obliquity-related SST maxima (minima) most likely correspond to obliquity maxima (minima), because this configuration also increases (reduces) the seasonal contrast. Pronounced SST minima concurred with dust (Fe/Al) and productivity (Ba_{bio}) maxima.

7.2.1 Precession phasing of upwelling and dust input

The large SST fluctuations of ~4°C at a low latitude suggest a periodic influence of upwelling of colder water. The temperature fluctuations could be related to variations in the degree of upwelling and/or variations in temperature of the upwelled water related to its source area. Upwelling likely occurred seasonally and depended on the position of the ITCZ. Around ~17 Ma, Site 959 was located in the southern hemisphere at a latitude ~5° more south than today. Likely, the more southerly position of the Guinea coast prevented the inflow of the NECC and EUC into the Gulf of Guinea, the establishment of the Guinea Current, and thus the establishment of coastal upwelling during boreal summer (Norris, 1998a; Wagner, 2002). In this scenario, the westward flowing SEC would be the main current in the Gulf of Guinea. Therefore, coastal upwelling more likely occurred during boreal winter in response to the southward displacement of the ITCZ and westward flowing surface winds. This suggests that SST minima occurred during precession maxima (NH summer insolation minima), when the ITCZ was in a more/prolonged southerly position compared to precession minima.

Aeolian dust input depends on dust production and transportation, which in turn depend on vegetation cover (aridity), availability of fine-grained sediments, and wind direction and strength (Trauth et al., 2009). This means that dust maxima can be related to strengthened NE winter trades and/or increased aridity of North Africa. In North Africa, precipitation and vegetation cover increased during NH summer insolation maxima and decreased during NH summer insolation minima (Bosmans et al., 2015a; Trauth et al., 2009). This suggests that dust peaks occurred during precession maxima (NH summer insolation minima). This is in agreement with the most likely precession phasing of SST minima concurring with Fe/Al maxima. Larger scale SST minima were related to eccentricity minima, and most likely, obliquity minima. Indeed, this configuration leads to lowest NH summer insolation and thus increased aridity and dust production.

This phasing differs (partly) from that assumed in Tiedemann et al. (1994) and Vallé et al. (2017). Tiedemann et al. (1994) linked Pliocene dust flux maxima off West Africa to eccentricity maxima and precession maxima, the latter in agreement with the phase relation assumed here. Vallé et al. (2017) followed the approach of Tiedemann et al. (1994) and tuned Late Miocene to Early Pleistocene dust maxima at Site 959 to eccentricity maxima. However, Vallé et al. (2017) linked dust flux maxima to precession minima (NH insolation maxima). This

interpretation was based on the correlation of dust (Fe) maxima to high values of benthic $\delta^{18}O$, linked to global ice volume (Vallé et al., 2017). However, the resolution (>10 kyr) of the benthic $\delta^{18}O$ record seems too low to determine the relation relative to precession. Additionally, they linked dust maxima to obliquity maxima (see Figure 8 in Vallé et al., 2017), which likely correspond to periods with reduced ice volume as summer insolation increases and thus lower values of benthic $\delta^{18}O$. This is contrast to their correlation of dust maxima to high values of benthic $\delta^{18}O$.

7.2.2 Leads and lags

At the precession period, bulk carbonate $\delta^{18}O$ and -TEX_{86}-SST are approximately in phase, suggesting that precession-scale changes in bulk carbonate $\delta^{18}O$ are mainly related to temperature changes in the (sub)surface waters. It is not clear why $\delta^{18}O$ leads -TEX_{86}-SST significantly (by 13.5 kyr) at the obliquity period. Bulk carbonate $\delta^{13}C$ and Ba_{bio} are approximately in phase, lagging -TEX_{86}-SST by ~2 kyr. Although bulk carbonate $\delta^{13}C$ slightly leads Ba_{bio} by 0.1 kyr, this 'in-phase' relationship suggests that enhanced productivity resulted in increased burial of organic C relative to $CaCO_3$, thereby increasing oceanic $\delta^{13}C$ and bulk carbonate $\delta^{13}C$ (Ma et al., 2011).

The pronounced peaks in the Ba_{bio} record correspond to darker layers related to diatomites, which have high abundances of diatoms, radiolarians and other siliceous components (Mascle et al., 1996). Diatom blooms are associated with upwelling systems and dust deposition (Calil et al., 2011). The Ba_{bio} peaks concur with Fe/Al maxima and SST minima, meaning increased productivity could be related to increased delivery of nutrients via dust and/or upwelling. At precession and obliquity periods, -TEX_{86}-SST leads Ba_{bio} by 2.1 and 0.3 kyr, respectively, while Fe/Al slightly lags Ba_{bio} by 0.4 and 0.1 kyr, respectively. This means that (export) productivity responded to upwelling on delay or, considering uncertainties in the phases, responded approximately in phase to dust input. Fe/Al peaks lag SST minima by 2.5 kyr and 0.4 kyr at the period of precession and obliquity, respectively. This indicates that upwelling might have responded more directly to changes in insolation, while it took more time for North Africa to become arid enough to deliver dust to Site 959.

V/Al and -$CaCO_3$ lag Ba_{bio} at the precession period by 2.2 and 2.4 kyr and at the obliquity period by 4 and 0.4 kyr, respectively. Thus, increased productivity resulted in increased decomposition of organic matter at the sea floor, resulting in dysoxic-suboxic and more corrosive bottom waters.

MS lags Ba_{bio} by 5.3 kyr, Fe/Al by 4.9 kyr and -$CaCO_3$ by 2.9 kyr at the precession period. This phasing of MS might be related to dilution of magnetic minerals by detrital (quartz) input, biogenic silica, and $CaCO_3$ (Larrasoaña et al., 2008). This could explain in the occurrence of MS maxima in between productivity/dust maxima and $CaCO_3$ maxima.

7.2.3 Eccentricity pacing

Before the MCO (~17.4-17 Ma) and in the later part of the MCO (~16.5-15.4 Ma), SST at Site 959 was strongly paced by ~100 kyr eccentricity. The ~100 kyr SST cycles were relatively symmetrical during the MCO, indicating a direct response to orbital insolation forcing. However, SST varied asymmetrically before the MCO, indicating a non-linear response to insolation forcing and the influence of additional processes/feedbacks.

The intensity or duration of upwelling must have varied significantly to produce the large SST fluctuations of ~4°C observed at Site 959. This suggests that wind strength varied significantly or that wind direction was favourable for upwelling for a prolonged period of time. However, as SST minima are linked to a reduced seasonal contrast (obliquity and eccentricity

minima), wind strength most likely did not increase significantly and increased upwelling might be related to a seasonally more stable position of the ITCZ.

Before the MCO (~17.4-17 Ma), Fe/Al, Ba_{bio} and V/Al were also strongly paced by ~100 kyr eccentricity. Large Fe/Al peaks occurred during pronounced SST minima, just before the rapid increase in SST in response to eccentricity maxima. However, between these large peaks variation of Fe/Al was small, suggesting that North Africa did not become arid enough (or winds strong enough) for significant amounts of dust to be delivered to Site 959. Indeed, modelling studies suggest that the North African climate was mostly semiarid and was not very sensitive to orbital changes in insolation during the Early Miocene (Zhang et al., 2014).

7.2.4 Early MCO obliquity pacing

After the onset of the MCO, between ~17 and ~16.5 Ma, the climate was more dynamic and dominated by obliquity and precession. The increased variance of Fe/Al compared to the pre-MCO interval suggests that the North African climate was overall more arid and more sensitive to changes in astronomical insolation forcing. The second-highest Fe/Al peak occurred around ~16.9 Ma, suggesting significantly more arid conditions and/or greater wind speeds at the start of the MCO.

Strong obliquity pacing is observed in records of SST, Fe/Al, Ba_{bio}, V/Al and $CaCO_3$. Relatively large Fe/Al and Ba_{bio} peaks occurred during pronounced SST minima, most likely related to obliquity minima in combination with precession maxima. The lower SSTs during obliquity minima might have reduced moisture transport to North Africa (Van der Ent & Savenije, 2013), amplifying the aridity and dust production. However, moisture transport mainly occurs during summer while upwelling (and thus lowest SST) is expected to have occurred during winter. The Ba_{bio} record shows a stronger obliquity signal compared to the records of TEX_{86}-SST and Fe/Al. This might be related to the increased input of nutrients through both dust delivery and upwelling during obliquity minima, amplifying productivity and thus the Ba_{bio} signal. Additionally, Ba_{bio} might have responded in a non-linear way to changes in nutrient delivery, maybe through processes of Ba_{bio} formation, transport and burial.

The influence of obliquity on low-latitude insolation is very small, however, it can affect low-latitude climate through its influence on inter-hemispheric insolation gradients (Bosmans et al., 2015b). Obliquity maxima increase the inter-tropical insolation gradient by increasing insolation in one hemisphere and decreasing insolation in the other hemisphere at the same time (and vice versa). It is shown that moisture transport to North Africa is reduced during obliquity minima (Bosmans et al., 2015b), increasing aridity and dust production. Additionally, the subdued northward migration of the ITCZ during obliquity minima likely stimulated coastal upwelling, thereby further reducing SSTs. However, could this direct forcing through changes in the inter-hemispheric insolation gradient solely be responsible for the strong obliquity signal observed in the proxy records?

The interval with strong obliquity pacing corresponds to a node in eccentricity (~2.4 Myr minimum). During this node, the amplitude of the ~100 kyr cycle is reduced, making the influence of obliquity relatively more important. Between ~16.9 and ~16.7 Ma, eccentricity remained relatively high due to ~400 kyr eccentricity modulation, resulting in a relatively long period of high seasonality with high-amplitude changes at the precession-scale. During ~400 kyr eccentricity minima, the relative influence of obliquity also increases due to low values of eccentricity. Indeed, increased obliquity influence is observed during these ~400 kyr minima in the SST record. Still, during the ~17-16.5 Ma interval, the obliquity signal in the proxy records is stronger than seen in curves of low-latitude insolation or inter-hemispheric insolation

gradients. Moreover, a strong obliquity signal is not present in the $\delta^{13}C$ record during this interval. This suggests an influence of remote high-latitude insolation changes.

7.3 High-latitude (glacial) influence

The asymmetry of ~100 kyr SST cycles before the MCO (~17.4-17 Ma) and the strong influence of obliquity at the beginning of the MCO (~17-16.5 Ma) suggest that the low-latitude climate was influenced by high-latitude (glacial) climate variability.

Before the MCO, ~100 kyr SST cycles are characterized by a rapid increase in response to eccentricity maxima followed by a gradual decrease with lower eccentricity, punctuated by smaller variations related to precession and obliquity. The asymmetry of the ~100 kyr cycles indicates a non-linear response to insolation forcing. Asymmetric, sawtooth-shaped cycles are typical for glacial cycles of the Late Pleistocene (Lisiecki & Raymo, 2007) and are also found in an Early Miocene benthic foraminiferal $\delta^{18}O$ record from Walvis Ridge, linked to prolonged ice sheet growth on Antarctica and subsequent rapid retreat (Liebrand et al., 2017). This suggests that, at least before ~17 Ma, SST at Site 959 was influenced by glacial-interglacial variability, possibly through changes in atmospheric or oceanic circulation.

Van der Weijst et al. (2021 preprint) linked Pliocene TEX_{86} variability at Site 959 to Antarctic Intermediate Water (AAIW), which is formed at the Antarctic Polar Front. During the Pliocene/Pleistocene, AAIW formation was related to the strength of the westerlies and extent of sea ice, which increased in response to colder middle/high southern latitudes. Tagliaro et al. (2021) showed that the Southern Ocean was very sensitive to ~100 and ~400 kyr fluctuation of the Antarctic Ice Sheet (AIS) during the Early Miocene. Therefore, it could be possible that pre-MCO SST at Site 959 was influenced by (proto-)AAIW, linking tropical SST changes to glacial-interglacial variability. In this case, changes in Southern Ocean dynamics during glacials resulted in an expansion and/or decreased temperature of AAIW, decreasing the temperature of upwelled water in the Gulf of Guinea. SH glacials occurred during SH summer insolation minima, which agrees with the phasing of SST minima during eccentricity and obliquity minima but disagrees with the expected precession phase of SST minima. Possibly, this discrepancy is related to the mechanism behind coastal upwelling in the Gulf of Guinea. In this scenario, upwelling itself would be related to local low-latitude forcing while the temperature of upwelled waters would be related to southern high-latitude forcing and glacial-interglacial variability.

Large Fe/Al peaks only occurred during peak glacial conditions. Glacial conditions might have affected North African aridity (or wind strength) through changes in atmospheric/oceanic circulation or the lowering of atmospheric CO_2 concentrations.

The strong obliquity signal recorded in records from Site 959, suggest that the climate at southern high latitudes was paced by obliquity during the early MCO (~17-16.5 Ma). SST cycles were relatively symmetrical during the MCO, indicating a more direct response to orbital forcing. During the MCO, the AIS was probably small and restricted to the inner continent (Colleoni et al., 2018) and southern-derived deep waters retracted (Tagliaro et al., 2021). During ~400 kyr maxima, ice volume might have been reduced to near ice-free conditions (Miller et al., 2020). A smaller AIS could have been more sensitive and respond more directly to changes in insolation. However, its influence on the surrounding climate probably decreased. It is not clear if the formation of (proto-)AAIW could be dependent on high-latitude insolation changes without the influence of a large ice sheet.

The Early/Middle Miocene SST record of Site 959 shows that in order to interpret SST changes and determine climate sensitivity it is important to understand where the SST signal

derived from and which processes were involved. In order to do so, high-resolution records are needed that capture the full variation over orbital time-scales.

7 Conclusions

The high-resolution Early/Middle Miocene (~17.4-15.4 Ma) records from Site 959 reveal well-expressed orbital cyclicity related to frequencies of precession, obliquity and eccentricity. The interval before the MCO (~17.4-17 Ma) is dominated by strong variability related to ~100 kyr eccentricity, punctuated by lower-amplitude fluctuations related to precession and obliquity. The TEX_{86}-SST record reveals asymmetrical ~100 kyr cycles, suggesting a link to glacial-interglacial variability. The interval between ~17 and ~16.5 Ma, after the onset of the MCO, is characterized by high-amplitude fluctuations related to obliquity and corresponds to a node in eccentricity (~2.4 Myr eccentricity minimum). The influence of obliquity is expressed as the amplification of every second or third precession cycle, resulting in an average cyclicity of ~50 kyr. The influence of high-latitude processes might be needed to explain the strong obliquity signal. The interval between ~16.5 and ~15.4 Ma is again strongly influenced by ~100 kyr eccentricity. The ~100 kyr TEX_{86}-SST cycles are relatively symmetrical, suggesting a more direct response to orbital forcing compared to the pre-MCO interval. The influence of obliquity is recognized during ~400 kyr eccentricity minima.

TEX_{86}-SST minima were likely related to phases of intensified/prolonged upwelling in the Gulf of Guinea and concurred with Fe/Al maxima, interpreted as increased dust input from North Africa, and Ba_{bio} maxima, linked to increased (export) productivity due to increased nutrient delivery. At least before ~17 Ma, TEX_{86}-SST was linked with glacial-interglacial variability possibly through the supply of southern-sourced intermediate water. Lowest TEX_{86}-SST occurred during eccentricity minima and most likely obliquity minima, as both reduce seasonal contrast. Probably, TEX_{86}-SST minima, Fe/Al maxima and Ba_{bio} maxima corresponded to precession maxima (NH insolation minima) as this configuration would result in a more/prolonged southerly position of the ITCZ, favouring coastal upwelling in the Gulf of Guinea and dust production in North Africa.

References

Akinnigbagbe, A.E., Han, X., Fan, W., Tang, Y., Adeleye, A.O., Jimoh, R.O., & Lou, Z. (2018). Variations in terrigenous input into the eastern equatorial Atlantic over 120ka: Implications on Atlantic ITCZ migration. *Journal of African Earth Sciences*, 147, 220–227. https://doi.org/10.1016/j.jafrearsci.2018.06.010

Basile, C., Mascle, J., Popoff, M., Bouillin, J.P., & Mascle , G. (1993). The Ivory Coast-Ghana transform margin: a marginal ridge structure deduced from seismic data. *Tectonophysics*, 222(1), 1–19. https://doi.org/10.1016/0040-1951(93)90186-N

Beckmann, B., Flögel, S., Hofmann, P., Schulz, M., & Wagner, T. (2005). Orbital forcing of Cretaceous river discharge in tropical Africa and ocean response. *Nature*, 437, 241–244. https://doi.org/10.1038/nature03976

Blaga, C.I., Reichart, G.-J., Heiri, O., & Sinninghe Damsté, J.S. (2009). Tetraether membrane lipid distributions in water-column particulate matter and sediments: a study of 47 European lakes along a north-south transect. *Journal of Paleolimnology*, 41, 523–540. https://doi.org/10.1007/s10933-008-9242-2

Bosmans, J.H.C., Drijfhout, S.S., Tuenter, E., Hilgen, F.J., & Lourens, L.J. (2015a). Response of the North African summer monsoon to precession and obliquity forcings in the EC-Earth GCM. *Climate Dynamics*, 44, 279–297. https://doi.org/10.1007/s00382-014-2260-z

Bosmans, J.H.C., Hilgen, F.J., Tuenter, E., & Lourens, L.J. (2015b). Obliquity forcing of low-latitude climate. *Climate of the Past*, 11(10), 1335–1346. https://doi.org/10.5194/cp-11-1335-2015

Bozzano, G., Kuhlmann, H., & Alonso, B. (2002). Storminess control over African dust input to the Moroccan Atlantic margin (NW Africa) at the time of maxima boreal summer insolation: a record of the last 220 kyr. *Palaeogeography, Palaeoclimatology, Palaeoecology*, 183(1–2), 155–168. https://doi.org/10.1016/S0031-0182(01)00466-7

Burls, N.J., Bradshaw, C.D., de Boer, A.M., Herold, N., Huber, M., Pound, M., Donnadieu, Y., Farnsworth, A., Frigola, A., Gasson, E., von der Heydt, A.S., Hutchinson, D.K., Knorr, G., Lawrence, K.T., Lear, C.H., Li, X., Lohmann, G., Lunt, D.J., Marzocchi, A., Prange, M., Riihimaki, C.A., Sarr, A.-C., Siler, N., & Zhang, Z. (2021). Simulating Miocene warmth: Insights from an opportunistic multi-Model ensemble (MioMIP1). *Paleoceanography and Paleoclimatology*, 36(5), 1–40. https://doi.org/10.1029/2020PA004054

Calil, P.H.R., Doney, S.C., Yumimoto, K., Eguchi, K., & Takemura, T. (2011). Episodic upwelling and dust deposition as bloom triggers in low-nutrient, low-chlorophyll regions. *Journal of Geophysical Research,* 116(C6). https://doi-org.proxy.library.uu.nl/10.1029/2010JC006704

Calvert, S.E., & Pedersen, T.F. (2007). Chapter Fourteen Elemental Proxies for Palaeoclimatic and Palaeoceanographic Variability in Marine Sediments: Interpretation and Application. In *Developments in Marine Geology*, 1, 567–644. https://doi.org/10.1016/S1572-5480(07)01019-6

Colleoni, F., de Santis, L., Montoli, E., Olivo, E., Sorlien, C.C., Bart, P.J., Gasson, E.G.W., Bergamasco, A., Sauli, C., Wardell, N., & Prato, S. (2018). Past continental shelf

evolution increased Antarctic ice sheet sensitivity to climatic conditions. *Scientific Reports*, 8(11323), 1–12. https://doi.org/10.1038/s41598-018-29718-7

Cramer, B.S., Wright, J.D., Kent, D.V., & Aubry, M.-P. (2003). Orbital climate forcing of $\delta^{13}C$ excursions in the late Paleocene-early Eocene (chrons C24n-C25n). *Paleoceanography and Paleoclimatology*, 18(4). https://doi-org.proxy.library.uu.nl/10.1029/2003PA000909

Djakouré, S., Penven, P., Bourlès, B., Koné, V., & Veitch, J. (2017). Respective roles of the Guinea current and local winds on the coastal upwelling in the northern Gulf of Guinea. *Journal of Physical Oceanography*, 47(6), 1367–1387. https://doi.org/10.1175/JPO-D-16-0126.1

Dymond, J., Suess, E., & Lyle, M. (1992). Barium in Deep-Sea Sediment: A Geochemical Proxy for Paleoproductivity. *Paleoceanography*, 7(2), 163–181. https://doi.org/10.1029/92PA00181

Ent, Van Der, R.J., & Savenije, H.H.G. (2013). Oceanic sources of continental precipitation and the correlation with sea surface temperature. *Water Resources Research*, 49(7), 3993–4004. https://doi.org/10.1002/wrcr.20296

Flower, B.P., & Kennett, J.P. (1993). Relations between Monterey Formation deposition and middle Miocene global cooling: Naples Beach section, California. *Geology*, 21(10), 877–880. https://doi.org/10.1130/0091-7613(1993)021<0877:RBMFDA>2.3.CO;2

Foster, G.L., Lear, C.H., & Rae, J.W.B. (2012). The evolution of pCO_2, ice volume and climate during the middle Miocene. *Earth and Planetary Science Letters*, 341–344, 243–254. https://doi.org/10.1016/j.epsl.2012.06.007

Ganeshram, R.S., François, R., Commeau, J., & Brown-Leger, S.L. (2003). An experimental investigation of barite formation in seawater. *Geochimica et Cosmochimica Acta*, 67(14), 2599–2605. https://doi.org/10.1016/S0016-7037(03)00164-9

Gingele, F., & Dahmke, A. (1994). Discrete barite particles and barium as tracers of paleoproductivity in south Atlantic sediments. *Paleoceanography*, 9(1), 151–168. https://doi.org/10.1029/93PA02559

Giorgioni, M., Weissert, H., Bernasconi, S.M., Hochuli, P.A., Coccioni, R., & Keller, C.E. (2012). Orbital control on carbon cycle and oceanography in the mid-Cretaceous greenhouse. *Paleoceanography and Paleoclimatology*, 27(1). https://doi-org.proxy.library.uu.nl/10.1029/2011PA002163

Govin, A., Holzwarth, U., Heslop, D., Ford Keeling, L., Zabel, M., Mulitza, S., Collins, J.A., & Chiessi, C.M. (2012). Distribution of major elements in Atlantic surface sediments (36°N-49°S): Imprint of terrigenous input and continental weathering. *Geochemistry, Geophysics, Geosystems*, 13(1), 1–23. https://doi.org/10.1029/2011GC003785

Herbert, T.D., Lawrence, K.T., Tzanova, A., Peterson, L.C., Caballero-Gill, R., & Kelly, C.S. (2016). Late Miocene global cooling and the rise of modern ecosystems. *Nature Geoscience*, 9, 843-847. https://doi-org.proxy.library.uu.nl/10.1038/ngeo2813

Hinsbergen, van, D.J.J., de Groot, L.V., van Schaik, S.J., Spakman, W., Bijl, P.K., Sluijs, A., Langereis, C.G., & Brinkhuis, H. (2015). A paleolatitude calculator for paleoclimate studies. *PLoS ONE*, 10(6). https://doi.org/10.1371/journal.pone.0126946

Holbourn, A., Kuhnt, W., Clemens, S., Prell, W., & Andersen, N. (2013). Middle to late Miocene stepwise climate cooling: Evidence from a high-resolution deep water isotope curve

spanning 8 million years. *Paleoceanography*, 28(4), 688–699. https://doi.org/10.1002/2013PA002538

Holbourn, A., Kuhnt, W., Kochhann, K.G.D., Andersen, N., & Meier, K.J.S. (2015). Global perturbation of the carbon cycle at the onset of the Miocene Climatic Optimum. *Geology*, 43(2), 123–126. https://doi.org/10.1130/G36317.1

Holbourn, A., Kuhnt, W., Lyle, M., Schneider, L., Romero, O., & Andersen, N. (2014). Middle Miocene climate cooling linked to intensification of eastern equatorial Pacific upwelling. *Geology*, 42(1), 19–22. https://doi.org/10.1130/G34890.1

Holbourn, A., Kuhnt, W., Schulz, M., Flores, J.A., & Andersen, N. (2007). Orbitally-paced climate evolution during the middle Miocene "Monterey" carbon-isotope excursion. *Earth and Planetary Science Letters*, 261(3–4), 534–550. https://doi.org/10.1016/j.epsl.2007.07.026

Hopmans, E.C., Weijers, J.W. H., Schefuß, E., Herfort, L., Sinninghe Damsté, J.S., & Schouten, S. (2004). A novel proxy for terrestrial organic matter in sediments based on branched and isoprenoid tetraether lipids. *Earth and Planetary Science Letters*, 224(1–2), 107–116. https://doi.org/10.1016/j.epsl.2004.05.012

Hounslow, M.W., White, H.E., Drake, N.A., Salem, M.J., El-Hawat, A., McLaren, S.J., Karloukovski, V., Noble, S.R., & Hlal, O. (2017). Miocene humid intervals and establishment of drainage networks by 23 Ma in the central Sahara, southern Libya. *Gondwana Research*, 45, 118–137. https://doi.org/10.1016/j.gr.2016.11.008

IPCC (2021). Summary for Policymakers. In: *Climate Change 2021: The Physical Science Basis. Contribution of Working Group I to the Sixth Assessment Report of the Intergovernmental Panel on Climate Change* [Masson-Delmotte, V., P. Zhai, A. Pirani, S. L. Connors, C. Péan, S. Berger, N. Caud, Y. Chen, L. Goldfarb, M. I. Gomis, M. Huang, K. Leitzell, E. Lonnoy, J.B.R. Matthews, T. K. Maycock, T. Waterfield, O. Yelekçi, R. Yu and B. Zhou (eds.)]. Cambridge University Press. In Press.

Kasten, S., Haese, R.R., Zabel, M., Ruhlemann, C., & Schulz, H.D. (2001). Barium peaks at glacial terminations in sediments of the equatorial Atlantic Ocean-relicts of deglacial productivity pulses? *Chemical Geology*, 175 (3–4), 635-651. https://doi.org/10.1016/S0009-2541(00)00377-6

Kim, J.H., van der Meer, J., Schouten, S., Helmke, P., Willmott, V., Sangiorgi, F., Koç, N., Hopmans, E.C., & Sinninghe Damsté, J.S. (2010). New indices and calibrations derived from the distribution of crenarchaeal isoprenoid tetraether lipids: Implications for past sea surface temperature reconstructions. *Geochimica et Cosmochimica Acta*, 74(16), 4639–4654. https://doi.org/10.1016/j.gca.2010.05.027

Larrasoaña, J.C., Roberts, A.P., & Rohling, E.J. (2008). Magnetic susceptibility of eastern Mediterranean marine sediments as a proxy for Saharan dust supply? *Marine Geology*, 254 (3-4), 224-229. https://doi.org/10.1016/j.margeo.2008.06.003

Larrasoaña, J.C., Roberts, A.P., Rohling, E.J., Winklhofer, M., & Wehausen, R. (2003). Three million years of monsoon variability over the northern Sahara. *Climate Dynamics*, 21, 689–698. https://doi.org/10.1007/s00382-003-0355-z

Li, M., Hinnov, L., & Kump, L. (2019). Acycle: Time-series analysis software for paleoclimate research and education. *Computers and Geosciences*, 127, 12–22. https://doi.org/10.1016/j.cageo.2019.02.011

Liebrand, D., Beddow, H.M., Lourens, L.J., Pälike, H., Raffi, I., Bohaty, S.M., Hilgen, F.J., Saes, M.J.M., Wilson, P.A., van Dijk, A.E., Hodell, D.A., Kroon, D., Huck, C.E., & Batenburg, S.J. (2016). Cyclostratigraphy and eccentricity tuning of the early Oligocene through early Miocene (30.1–17.1 Ma): Cibicides mundulus stable oxygen and carbon isotope records from Walvis Ridge Site 1264. *Earth and Planetary Science Letters*, 450, 392–405. https://doi.org/10.1016/j.epsl.2016.06.007

Liebrand, D., de Bakker, A.T. M., Beddow, H.M., Wilson, P.A., Bohaty, S.M., Ruessink, G., Pälike, H., Batenburg, S.J., Hilgen, F.J., Hodell, D.A., Huck, C.E., Kroon, D., Raffi, I., Saes, M.J.M., van Dijk, A.E., & Lourens, L.J. (2017). Evolution of the early Antarctic ice ages. *Proceedings of the National Academy of Sciences of the United States of America*, 114(15), 3867–3872. https://doi.org/10.1073/pnas.1615440114

Linke, C., Möhler, O., Veres, A., Mohácsi, A, Bozóki, Z., Szabó, G., & Schnaiter, M. (2006). Optical properties and mineralogical composition of different Saharan mineral dust samples: a laboratory study. *Atmos. Chem. Phys.*, 6(11), 3315-3323. https://doi.org/10.5194/acp-6-3315-2006

Lisiecki, L.E., & Raymo, M.E. (2007). Plio-Pleistocene climate evolution: trends and transitions in glacial cycle dynamics. *Quaternary Science Reviews*, 26(1–2), 56–69. https://doi.org/10.1016/j.quascirev.2006.09.005

Ma, W., Tian, J., Li, Q., & Wang, P. (2011). Simulation of long eccentricity (400-kyr) cycle in ocean carbon reservoir during Miocene Climatic Optimum: Weathering and nutrient response to orbital change. *Geophysical Research Letters*, 38(10). https://doi-org.proxy.library.uu.nl/10.1029/2011GL047680

Martinez-Ruiz, F., Kastner, M., Gallego-Torres, D., Rodrigo-Gámiz, M., Nieto-Moreno, V., & Ortega-Huertas, M. (2015). Paleoclimate and paleoceanography over the past 20,000 yr in the Mediterranean Sea Basins as indicated by sediment elemental proxies. *Quaternary Science Reviews*, 107(1), 25–46. https://doi.org/10.1016/j.quascirev.2014.09.018

Mascle, J., Lohmann, G.P., Clift, P.D., et al. (1996). *Proceedings of the Ocean Drilling Program, Initial Reports*, 159: College Station, TX (Ocean Drilling Program).

Miller, K.G., Browning, J.V, Schmelz, W.J., Kopp, R.E., Mountain, G.S., & Wright, J.D. (2020). Cenozoic sea-level and cryospheric evolution from deep-sea geochemical and continental margin records. *Science Advances*, 6(20). https://doi.org/10.1126/sciadv.aaz1346

Modestou, S.E., Leutert, T.J., Fernandez, A., Lear, C.H., & Meckler, A.N. (2020). Warm middle Miocene Indian Ocean bottom water temperatures: Comparison of clumped isotope and Mg/Ca-based estimates. *Paleoceanography and Paleoclimatology*, 35(11). https://doi-org.proxy.library.uu.nl/10.1029/2020PA003927

Moskowitz, B.M., Reynolds, R.L., Goldstein, H.L., Berquó, T.S., Kokaly, R.F., & Bristow, C.S. (2016). Iron oxide minerals in dust-source sediments from the Bodélé Depression, Chad: Implications for radiative properties and Fe bioavailability of dust plumes from the Sahara. *Aeolian Research*, 22, 93–106. https://doi.org/10.1016/j.aeolia.2016.07.001

Norris, R.D. (1998a). Miocene-Pliocene surface-water hydrography of the eastern equatorial Atlantic. In *Proceedings of the Ocean Drilling Program, Scientific Results*, 159, 539-555.

Norris, R.D. (1998b). Planktonic foraminifer biostratigraphy: eastern equatorial Atlantic. In *Proceedings of the Ocean Drilling Program, Scientific Results*, 159, 445-479.

Piela, C., Lyle, M., Marcantonio, F., Baldauf, J., & Olivarez Lyle, A. (2012). Biogenic sedimentation in the equatorial Pacific: Carbon cycling and paleoproduction, 12-24 Ma. *Paleoceanography*, 27(2). https://doi.org/10.1029/2011PA002236

Prospero, J.M., Ginoux, P., Torres, O., Nicholson, S.E., & Gill, T.E. (2002). Environmental characterization of global sources of atmospheric soil dust identified with the Nimbus 7 Total Ozone Mapping Spectrometer (TOMS) absorbing aerosol product. *Reviews of Geophysics*, 40(1), 2-1-2–31. https://doi.org/10.1029/2000RG000095

Reitz, A., Pfeifer, K., de Lange, G.J., & Klump, J. (2004). Biogenic barium and the detrital Ba/Al ratio: A comparison of their direct and indirect determination. *Marine Geology*, 204(3–4), 289–300. https://doi.org/10.1016/S0025-3227(04)00004-0

Rutsch, H.-J., Mangini, A., Bonani, G., Dittrich-Hannen, B., Kubik, P.W., Suter, M., & Segl, M. (1995). ^{10}Be and Ba concentrations in West African sediments trace productivity in the past. *Earth and Planetary Science Letters,* 133(1–2), 129-143. https://doi.org/10.1016/0012-821X(95)00069-O

Schouten, S., Hopmans, E.C., Schefuß, E., & Sinninghe Damsté, J.S. (2002). Distributional variations in marine crenarchaeotal membrane lipids: a new tool for reconstructing ancient sea water temperatures? *Earth and Planetary Science Letters*, 204(1–2), 265–274. https://doi.org/10.1016/S0012-821X(02)00979-2

Shafik, S., Watkins, D.K., & Chul Shin, I. (1998). Upper Cenozoic Calcareous Nannofossil Biostratigraphy Côte d'Ivoire-Ghana Margin, Eastern Equatorial Atlantic. In *Proceedings of the Ocean Drilling Program, Scientific Results*, 159, 509-523.

Sinninghe Damsté, J.S. (2016). Spatial heterogeneity of sources of branched tetraethers in shelf systems: The geochemistry of tetraethers in the Berau River delta (Kalimantan, Indonesia). *Geochimica et Cosmochimica Acta*, 186, 13–31. https://doi.org/10.1016/j.gca.2016.04.033

Sluijs, A., Frieling, J.,N. Inglis, G., Nierop, K.G.J., Peterse, F., Sangiorgi, F., & Schouten, S. (2020). Late Paleocene-early Eocene Arctic Ocean sea surface temperatures: Reassessing biomarker paleothermometry at Lomonosov Ridge. *Climate of the Past*, 16(6), 2381–2400. https://doi.org/10.5194/cp-16-2381-2020

Sosdian, S.M., & Lear, C.H. (2020). Initiation of the western Pacific warm pool at the Middle Miocene Climatic Transition? *Paleoceanography and Paleoclimatology*, 35(12). https://doi-org.proxy.library.uu.nl/10.1029/2020PA003920

Sosdian, S.M., Babila, T.L., Greenop, R., Foster, G.L., & Lear, C.H. (2020). Ocean Carbon Storage across the middle Miocene: a new interpretation for the Monterey Event. *Nature Communications*, 11. https://doi.org/10.1038/s41467-019-13792-0

Sosdian, S.M., Greenop, R., Hain, M.P., Foster, G.L., Pearson, P.N., & Lear, C.H. (2018). Constraining the evolution of Neogene ocean carbonate chemistry using the boron isotope pH proxy. *Earth and Planetary Science Letters*, 498, 362–376. https://doi.org/10.1016/j.epsl.2018.06.017

Steinthorsdottir, M., Coxall, H.K., de Boer, A.M., Huber, M., Barbolini, N., Bradshaw, C.D., Burls, N.J., Feakins, S.J., Gasson, E., Henderiks, J., Holbourn, A.E., Kiel, S., Kohn, M.J., Knorr, G., Kürschner, W.M., Lear, C.H., Liebrand, D., Lunt, D.J., Mörs, T., Pearson, P.N.,

Pound, M.J., Stoll, H., & Strömberg, C.A.E. (2021). The Miocene: The Future of the Past. *Paleoceanography and Paleoclimatology*, 36(4). https://doi.org/10.1029/2020PA004037

Steinthorsdottir, M., Vajda, V., & Pole, M. (2019). Significant transient pCO_2 perturbation at the New Zealand Oligocene-Miocene transition recorded by fossil plant stomata. *Palaeogeography, Palaeoclimatology, Palaeoecology*, 515, 152-161. https://doi.org/10.1016/j.palaeo.2018.01.039

Stoll, H.M., Guitian, J., Hernandez-Almeida, I., Mejia, M., Phelps, S., Polissar, P., Rosenthal, Y., Zhang, H., & Ziveri, P. (2019). Upregulation of phytoplankton carbon concentrating mechanisms during low CO_2 glacial periods and implications for the phytoplankton pCO_2 proxy. *Quaternary Science Reviews*, 208, 1-20. https://doi.org/10.1016/j.quascirev.2019.01.012

Stuut, J.B., Zabel, M., Ratmeyer, V., Helmke, P., Schefuß, E., Lavik, G., & Schneider, R. (2005). Provenance of present-day eolian dust collected off NW Africa. *Journal of Geophysical Research: Atmospheres*, 110(D4), 1–14. https://doi.org/10.1029/2004JD005161

Super, J.R., Thomas, E., Pagani, M., Huber, M., O'Brien, C., & Hull, P.M. (2018). North Atlantic temperature and pCO_2 coupling in the early-middle Miocene. *Geology*, 46(6), 519-522. https://doi.org/10.1130/G40228.1

Super, J.R., Thomas, E., Pagani, M., Huber, M., O'Brien, L., & Hull, P.M. (2020). Miocene evolution of North Atlantic sea surface temperature. *Paleoceanography and Paleoclimatology*, 35(5). https://doi-org.proxy.library.uu.nl/10.1029/2019PA003748

Tagliaro, G., Fulthorpe, C., Watkins, D., Brumsack, H., & Jovane, L. (2021). Southern Ocean carbonate dissolution paced by Antarctic Ice-Sheet expansion in the early Miocene. *Global and Planetary Change*, 202. https://doi.org/10.1016/j.gloplacha.2021.103510

Taylor, K.W.R., Huber, M., Hollis, C.J., Hernandez-Sanchez, M.T., & Pancost, R.D. (2013). Re-evaluating modern and Palaeogene GDGT distributions: Implications for SST reconstructions. *Global and Planetary Change*, 108, 158–174. https://doi.org/10.1016/j.gloplacha.2013.06.011

Tiedemann, R., Sarnthein, M., & Shackleton, N.J. (1994). Astronomic timescale for the Pliocene Atlantic $\delta^{18}O$ and dust flux records of Ocean Drilling Program Site 659. *Paleoceanography,* 9(4), 619–638. https://doi.org/10.1029/94PA00208

Trauth, M.H., Larrasoaña, J.C., & Mudelsee, M. (2009). Trends, rhythms and events in Plio-Pleistocene African climate. *Quaternary Science Reviews*, 28(5–6), 399–411. https://doi.org/10.1016/j.quascirev.2008.11.003

Vallé, F., Westerhold, T., & Dupont, L.M. (2017). Orbital-driven environmental changes recorded at ODP Site 959 (eastern equatorial Atlantic) from the Late Miocene to the Early Pleistocene. *International Journal of Earth Sciences*, 106, 1161–1174. https://doi.org/10.1007/s00531-016-1350-z

Vincent, E., & Berger, W.H. (1985). Carbon dioxide and polar cooling in the Miocene: The Monterey hypothesis. *The Carbon Cycle and Atmospheric CO_2: Natural Variations Archean to Present*, 32, 455–468. https://doi-org.proxy.library.uu.nl/10.1029/GM032p0455

Vleeschouwer, De, D., Vahlenkamp, M., Crucifix, M., & Pälike, H. (2017). Alternating Southern and Northern Hemisphere climate response to astronomical forcing during the past 35 m.y. *Geology*, 45(4), 375–378. https://doi.org/10.1130/G38663.1

Wagner, T. (1998). Pliocene-Pleistocene deposition of carbonate and organic carbon at Site 959: paleoenvironmental implications for the eastern equatorial Atlantic off the Ivory Coast/Ghana. In *Proceedings of the Ocean Drilling Program, Scientific Results*, 159, 557-574.

Wagner, T. (2002). Late Cretaceous to early Quaternary organic sedimentation in the eastern Equatorial Atlantic. *Palaeogeography, Palaeoclimatology, Palaeoecology*, 179(1–2), 113–147. https://doi.org/10.1016/S0031-0182(01)00415-1

Wang, P. (2009). Global monsoon in a geological perspective. *Chinese Science Bulletin*, 54, 1113-1136. https://doi-org.proxy.library.uu.nl/10.1007/s11434-009-0169-4

Weijers, J.W.H., Lim, K.L.H., Aquilina, A., Sinninghe Damsté, J.S., & Pancost, R.D. (2011). Biogeochemical controls on glycerol dialkyl glycerol tetraether lipid distributions in sediments characterized by diffusive methane flux. *Geochemistry, Geophysics, Geosystems*, 12(10). https://doi.org/10.1029/2011GC003724

Weijers, J.W.H., Schefuß, E., Kim, J.H., Sinninghe Damsté, J.S., & Schouten, S. (2014). Constraints on the sources of branched tetraether membrane lipids in distal marine sediments. *Organic Geochemistry*, 72, 14–22. https://doi.org/10.1016/j.orggeochem.2014.04.011

Weijers, J.W.H., Schouten, S., Spaargaren, O.C., & Sinninghe Damsté, J.S. (2006). Occurrence and distribution of tetraether membrane lipids in soils: Implications for the use of the TEX^{86} proxy and the BIT index. *Organic Geochemistry*, 37(12), 1680–1693. https://doi.org/10.1016/j.orggeochem.2006.07.018

Weijst, Van Der, C.M.H., van der Laan, K.J., Peterse, F., Reichart, G.-J., Schouten, S., Veenstra, T.J., & Sluijs, A. (2021 preprint). A fifteen-million-year surface-and subsurface-integrated TEX86 temperature record from the eastern equatorial Atlantic. *Climate of the Past*, prepint. https://doi.org/10.5194/cp-2021-92

Westerhold, T., Marwan, N., Drury, A.J., Liebrand, D., Agnini, C., Anagnostou, E., Barnet, J.S.K., Bohaty, S.M., de Vleeschouwer, D., Florindo, F., Frederichs, T., Hodell, D.A., Holbourn, A.E., Kroon, D., Lauretano, V., Littler, K., Lourens, L.J., Lyle, M., Pälike, H., Röhl, U., Tian, J., Wilkens, R.H., Wilson, P.A., & Zachos, J.C. (2020). An astronomically dated record of Earth's climate and its predictability over the last 66 million years. *Science*, 369(6509), 1383–1387. https://doi.org/10.1126/science.aba6853

Woodruff, F., & Savin, S.M. (1991). Mid-Miocene isotope stratigraphy in the deep sea: High-resolution correlations, paleoclimatic cycles, and sediment preservation. *Paleoceanography and Paleoclimatology*, 6(6), 755–806. https://doi-org.proxy.library.uu.nl/10.1029/91PA02561

Xiao, W., Wang, Y., Zhou, S., Hu, L., Yang, H., & Xu, Y. (2016). Ubiquitous production of branched glycerol dialkyl glycerol tetraethers (brGDGTs) in global marine environments: A new source indicator for brGDGTs. *Biogeosciences*, 13(20), 5883–5894. https://doi.org/10.5194/bg-13-5883-2016

Zhang, Y.G., Pagani, M., & Wang, Z. (2016). Ring Index: A new strategy to evaluate the integrity of TEX^{86} paleothermometry. *Paleoceanography*, 31(2), 220–232. https://doi.org/10.1002/2015PA002848

Zhang, Y.G., Pagani, M., Liu, Z., Bohaty, S.M., & DeConto, R. (2013). A 40-million-year history of atmospheric CO_2. *Philosophical Transactions of the Royal Society A*, 371, 20130096. https://doi.org/10.1098/rsta.2013.0096

Zhang, Y.G., Zhang, C.L., Liu, X.L., Li, L., Hinrichs, K.U., & Noakes, J.E. (2011). Methane Index: A tetraether archaeal lipid biomarker indicator for detecting the instability of marine gas hydrates. *Earth and Planetary Science Letters*, 307(3–4), 525–534. https://doi.org/10.1016/j.epsl.2011.05.031

Zhang, Z., Ramstein, G., Schuster, M., Li, C., Contoux, C., & Yan, Q. (2014). Aridification of the Sahara desert caused by Tethys Sea shrinkage during the Late Miocene. *Nature*, 513, 401–404. https://doi.org/10.1038/nature13705

Supplementary information

Calculation of GDGT indices

Several GDGT indices were calculated to assess potential biases in TEX_{86}-derived SSTs. The Ring Index (RI), based on the weighted average of cyclopentane moieties, was used to determine the potential influence of non-thermal factors and deviation from modern analogues (Zhang et al., 2016):

$$RI = \frac{(0 \times GDGT-0) + (1 \times GDGT-1) + (2 \times GDGT-2) + (3 \times GDGT-3) + (4 \times Cren) + (4 \times Cren')}{GDGT-0 + GDGT-1 + GDGT-2 + GDGT-3 + Cren + Cren'}$$

$$RI_{TEX} = (-0.77 \times TEX_{86}^{H}) + \left(3.32 \times {TEX_{86}^{H}}^{2}\right) + 1.59$$

$$\Delta RI = RI_{TEX} - RI$$

ΔRI values above |0.3| indicate a GDGT distribution that deviates from the modern TEX_{86}-RI relationship (Zhang et al., 2016). The Methane Index (MI) was used to quantify the contribution of anaerobic methanotrophic Euryarchaeota, represented by GDGT-1, -2, and -3, relative to Crenarchaeota, represented by crenarchaeol and its isomer (Zhang et al., 2011):

$$MI = \frac{GDGT-1 + GDGT-2 + GDGT-3}{GDGT-1 + GDGT-2 + GDGT-3 + Cren + Cren'}$$

MI values above 0.5 represent a dominance of GDGT-1, -2 and -3 over crenarchaeol, indicating a substantial contribution of anaerobic methanotrophic Euryarchaeota (Zhang et al., 2011). Additionally, the GDGT-2/crenarchaeol ratio was calculated to determine the contribution of anaerobic methanotrophic archaea (Weijers et al., 2011). The GDGT-0/crenarchaeol ratio was calculated, which indicates a substantial methanogenic origin of GDGT-0 for values above 2. (Blaga et al., 2009). The GDGT-2/GDGT-3 ratio was used to determine the contribution from archaea living in the deeper water column (Taylor et al., 2013). Values above 5 indicate contributions of deep water (>1000 m water depth) archaea (Taylor et al., 2013). The $\#rings_{tetra}$ (Sinninghe Damsté, 2016) and IIIa/IIa ratio (Xiao et al., 2016) were used to evaluate the source of branched GDGTs:

$$\#rings_{tetra} = \frac{Ib + (2 \times Ic)}{Ia + Ib + Ic}$$

$\#rings_{tetra}$ is low in sediments close to the river mouth (0.22), reaches the highest values in sediments on the shelf (0.83), and decreases gradually in deeper sediments (0.29) (Sinninghe Damsté, 2016). Terrestrially-derived branched GDGTs have lower IIIa/IIa values (<0.59 in soils) while marine-derived branched GDGTs have higher IIIa/IIa values (0.59-0.92 and >0.92 in marine sediments with and without significant terrestrial inputs, respectively) (Xiao et al., 2016).

Results of GDGT indices

The calculated GDGT ratios do not suggest TEX_{86} is affected by nonthermal processes.

The ΔRI is below |0.3| except for two values at 220.93 and 240.65 rmbsf. The MI is below 0.5 with values varying between 0.12 and 0.30. GDGT-2/Cren varies between 0.05 and 0.25. GDGT-0/Cren is below 2 with values varying between 0.08 and 0.64. GDGT-2/-3 varies between 2.97 and 5.69, except for two lower values (1.81 and 0.97) and two higher values (~6.5). 49 values are above 5, of which 39 occur in core 22X. High values correspond to both low and high SSTs. Values of #rings(tetra) vary between 0 and 0.68. IIIa/IIa varies between 1.18 and 4.25, except for one value of 0.51.

Results of additional elemental ratios

Records of the elemental ratios Ti/Al, K/Al, Mg/Al resemble the Fe/Al record, with clear maxima corresponding to clear Fe/Al peaks (Figure S1). Smaller peaks are present between the more pronounced peaks, although these smaller peaks do not always correlate well between the different elemental records. Noticeable in the Ti/Al record are the three large peaks >0.054 ppm in core 25X. Ti/Al varies between 0.036 and 0.078, Fe/Al between 0.33 and 1.22, K/Al between 0.069 and 0.151, Mg/Al between 0.079 and 0.191, and V/Al between 0.0011 and 0.0030 ppm. K/Al and Mg/Al values have the same order of magnitude, while some Fe/Al peaks an order of magnitude higher, Ti/Al values are an order of magnitude lower, and V/Al values are two orders of magnitude lower.

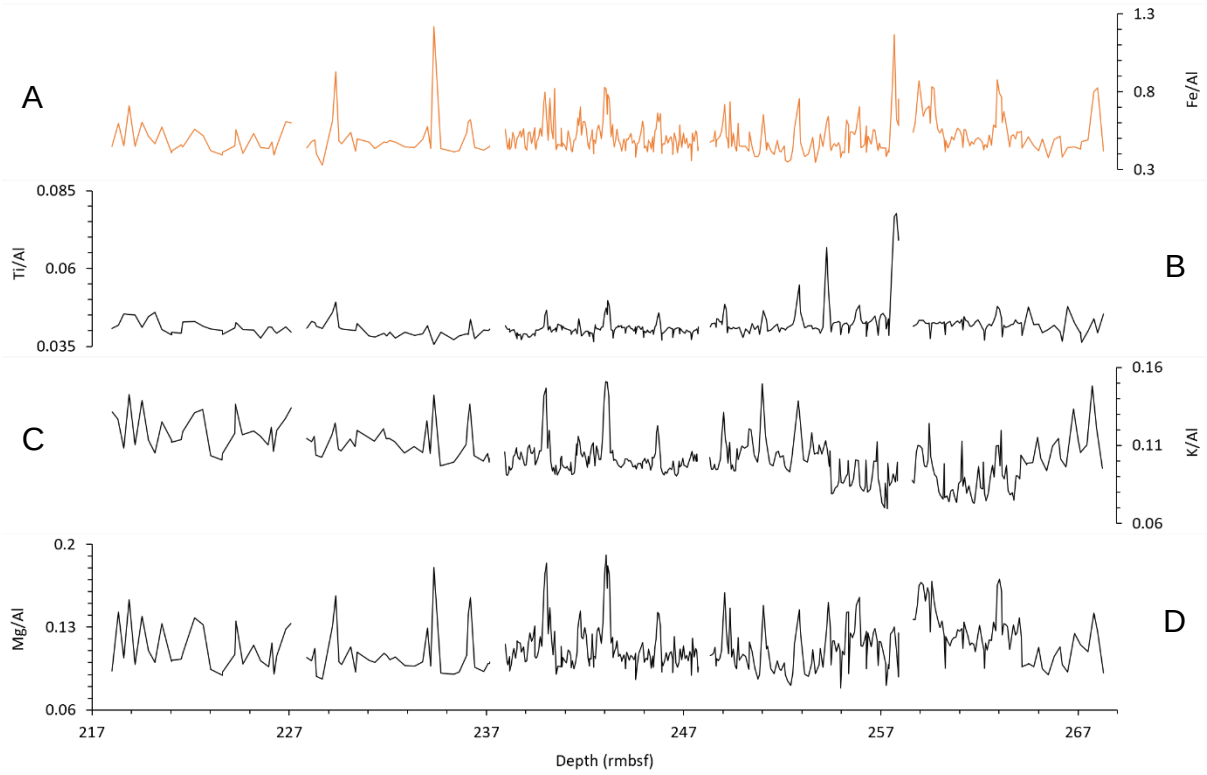

Figure S1. ODP Site 959 records Fe/Al (A), Ti/Al (B), K/Al (C) and Mg/Al (D) plotted against depth. The records span from ~268 to ~218 rmbsf corresponding to cores 26-22X.